Master's Degree in
Aerospace Engineering

Politecnico di Torino

Master's Degree Thesis

Implementation and Analysis of Far-Field Methodologies for Aerodynamic Force Decomposition in a Commercial CFD Software

Supervisors:

Prof. Domenic D'Ambrosio

Ph.D. Manuel Carreno Ruiz

Candidate:

Alessio Raffa

2022/2023

Abstract

The research for a more friendly environment is pushing engineering to its limits. Aeronautical field is no exception.

In this context new methods, called far-field methods, developed over the course of the years for the study of aerodynamic performances. The main aspects involved in these methodologies are the integration in the flow field and the decomposition of the aerodynamic resistance or drag into its phenomenological sources, the viscous, the wave and the lift-induced drag. This can lead to new wing designs and help to reduce the drag produced by an aircraft, meaning less fuel consumption and pollution. The difference with the classic approach of drag analysis, which is called near-field, is that this one involves an integration on the body surface and allows to breakdown the resistance into pressure and shear contributions.

This paper focuses the attention on the Computational Fluid Dynamics analysis and the aim is to evaluate the accuracy of these methodologies.

Initially various formulations, followed by a simulation and a first application of the methods are presented.

In the second part a deeper analysis is conducted, where the drag decomposition is applied to different cases, both two dimensional and three dimensional, showing all the aspects involved in a CFD simulation in order to perform the correct integration and post-processing for the study of the far-field methodologies.

Contents

List of Figures

List of Tables

Nomenclature

$\boldsymbol{\omega}$	vorticity vector
$\boldsymbol{\tau}$	viscous stress tensor
$\boldsymbol{f_{irr}}$	irreversible component of vector $\boldsymbol{f}$
$\boldsymbol{f_{rev}}$	reversible component of vector $\boldsymbol{f}$
$\boldsymbol{F}$	force vector
$\boldsymbol{i}$	unitary freestream direction vector
$\boldsymbol{l}$	Lamb-Vector
$\boldsymbol{n}$	normal vector
$\boldsymbol{V}$	velocity vector
$\dot{\boldsymbol{q}}$	heat flux
$\dot{\xi}$	heat absorbed per unit time and unit mass
γ	ratio of specific heats
∞	freestream state (subscript)
λ	mean free path
μ	dynamic viscosity
Ω	total volume of the control volume
Ω_v	volume of integration for the viscous drag
Ω_w	volume of integration for the wave drag
ρ	density
a	speed of sound
AMR	Adaptive Mesh Refinement
c	reference chord

C_p	specific pressure heat
C_v	specific volume heat
CD	drag coefficient, $CD = \frac{D}{0.5\rho_\infty u_\infty^2 S_{ref}}$
CFD	Computational Fluid Dynamics
CV	Control Volume
D	total drag
D_{ff}	far-field drag
D_f	friction drag
D_i	induced drag
D_{nf}	near-field drag
D_p	pressure drag
D_{sp}	spurious drag
D_{vw}	profile drag, sum of viscous and wave drag
D_v	viscous drag
D_w	wave drag
E	total energy per unit time
e	internal energy
H	total enthaply
h	enthaply
k	thermal conductivity
Kn	Knudsen number
L_{char}	characteristics length scale
M	Mach number
p	static pressure
p_0	total pressure
p_d	dynamic pressure
R	specific gas constant
$RANS$	Reynolds-Averaged Navier-Stokes

Re	Reynolds number
S	generic surface of integration
s	entropy
S_{body}	body surface for the integration
S_e	external surface of the control volume
S_{ref}	reference surface
S_{sw}	surface of integration for the wave drag
S_v	surface of integration for the viscous drag
S_w	wake plane
T	static temperature
t	time
u, v, w	velocity components in the aerodynamic reference frame
u_{irr}	irreversible axial velocity
V	generic volume of integration

Chapter 1

Introduction

In this first chapter it will be presented the general context in which the far-field methods take place and why they are used, followed by a presentation of the main equations that are used in the field of fluid dynamics, the Navier-Stokes equations.

1.1 Context

In a world that is moving towards ecology and environment respect, the aeronautical industry is no exception, in order to achieve a better standard of emissions but also from an economical point of view.

This has always been the case since the beginning of aviation, with engineers always trying to find better ways to improve fuel consumption and aircraft performance in general. There are different ways to achieve these results. Improve the propulsion system efficiency taking in consideration the bypass ratio for turbofan engines or use new technologies such as open rotors. Reduce the weight of the structure with innovative lightweight materials, especially carbon-fiber and other composite materials. Finally the aerodynamic performance can be enhanced. Here the main focus is on the drag or resistance, that is the force which opposes the aircraft motion caused by the pressure and the friction at the skin.

Designers can work in order to find the best fuselage or wing shape to minimize drag and this can lead to a better fuel consumption, so less costs and better overall performance of the aircraft. To be sure where to take an action on the design it is necessary to have a correct measurement of the forces in consideration, the drag already mentioned and the lift which is the force that allows the aircraft to sustain itself during the flight.

During the decades lot of experiments have been carried out. A good method to measure the force is the analysis through wind tunnel experiments, where the use of balances give the chance to measure directly the forces on the model. Other instruments can be probes in the wake, pressure probes, pressure sensitive paint on the skin, laser technologies such as Laser-Doppler-Velocimetry (LVD) and Particle-Image-Velocimetry (PIV). The problem with these practical experiments is that the use of wind tunnel requires a great amount of energy, time and costs. Moreover it is difficult

to make various models in case of small variations in the design, and tests at high speeds can lead to a very demanding facility.

This is the context where the development of numerical methods can be observed. Thanks to these methods the aerodynamic forces can be computed via Computational Fluid Dynamics (CFD) flow solutions. The use of CFD allows aerodynamic designers to make small variations on the design and have a relatively fast feedback from the solutions obtained numerically. To measure the forces the most direct methods are the so-called near-field methods, which give solutions through the integration of the friction and the pressure exerted by the fluid directly on the skin of the aircraft. With this approach it is possible to obtain the overall values of lift and drag, a breakdown in friction and pressure components, but the information about the phenomenological sources of the forces is not identified.

The aircraft experiences the forces in a free stream flow, but this concept can be also seen the other way around. The flow, encountering the aircraft which represents an obstacle, experiences different phenomena, shock wave, boundary layer, vortices. This phenomena lead to the far-field methods, where the idea is to integrate the stresses in the flow itself rather than on the skin, in this way the total drag can be computed and it can be decomposed in three phenomenological sources:

- *viscous drag*, caused by the stresses within the boundary layer around the body, and in its wake (fig. 1.1a);
- *wave drag*, due to the presence of shock waves in the flow field (fig. 1.1b);
- *induced drag*, given by the presence of vortices at the wing tips caused by the rotation of the lift (fig. 1.1c).

(a) Wake

(b) Cone shock

(c) Wingtip vortices

Figure 1.1: Drag sources

The viscous drag can be mitigate with the use of laminar wings and riblets which reduce the viscous stresses within the boundary layer (fig. 1.2a). The use of supercritical airfoil allows to reduce the strength of the shock during transonic cruise and as a consequence reduce the wave drag (fig. 1.2b). The induced drag can be reduced with the use of winglets at the wing tips (fig. 1.2c).

It is important to remember that these phenomena are interlinked, so the key here is to understand that the decomposition in each contribution is artificial and because of the complexity of the flow the physics of the problem is modeled in order to use the far-field methods.

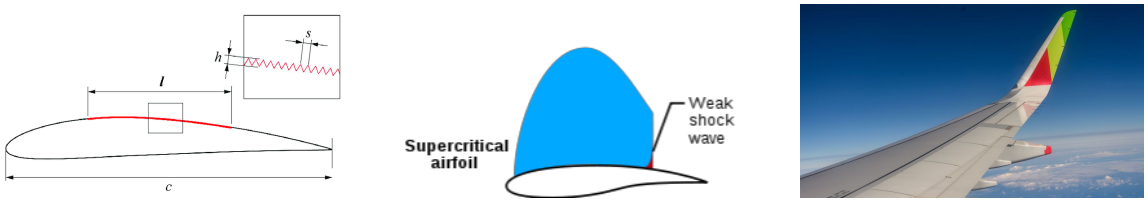

(a) Riblets (b) Supercritical airfoil (c) Winglet

Figure 1.2: Drag reduction systems

1.2 Navier-Stokes equations

The Navier-Stokes equations are the main equations in the field of fluid dynamics. A brief summary is here presented in order to better understand the concepts that will be discussed afterwards.

The fundamental form of the governing equations of the fluid dynamics is represented by the Boltzmann equations. The Navier-Stokes equations are the derivation through series expansion of order 1 and they express three basic physical principles: the mass is conserved, Newton's second law and the energy is conserved.

In order to properly use these equations the fluid has to be considered as a continuum, concept expressed by the Knudsen number Kn, defined as the ratio of the mean free path λ to a characteristic length scale L_{char} of the fluid mechanical system (1.1). Moreover they are subject to the boundary conditions of the problem in exam.

$$Kn = \frac{\lambda}{L_{char}} \tag{1.1}$$

To write the equations that expresses the three principles mentioned above, the concept of control volume (CV) is introduced. The control volume can be:

- *finite and fixed*, equations in integral and conservative form (fig. 1.3a);
- *finite and moving*, equations in integral and non-conservative form (fig. 1.3b);
- *infinitesimal and fixed*, equations in differential and conservative form (fig. 1.3c);
- *infinitesimal and moving*, equations in differential and non-conservative form (fig. 1.3d).

The fixed control volumes are crossed by the fluid whereas the control volumes that are moving with the fluid are always composed of the same fluid particles. The form of the control volume chosen gives different form of the equations, but the meaning of the physical principle remains the same, so one equation can be written in another form through mathematical manipulation. For the convenience of what will be discussed later with the presentation of the far-field methods, the three principles will be written in the integral and conservative form (finite and fixed control volume).

It is worth mentioning that there is a subtle difference between integral and differential form: the former admits discontinuities whereas the latter does not. It is clear that since the flow we want to analyze contains discontinuity such as shock waves, the integral form is the one to prefer.

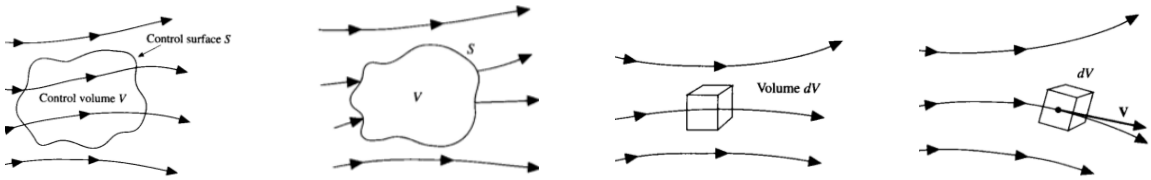

(a) Finite and fixed CV (b) Finite and moving CV (c) Infinitesimal and fixed CV (d) Infinitesimal and moving CV

Figure 1.3: Control volumes

1.2.1 Mass balance equation

The fluid crosses the control volume V which is surrounded by the control surface S. The physical principle states that the mass is conserved. The meaning of this is to say: the net flux of mass coming out from the control volume through surface S equals the reduction in time of the mass contained inside the control volume.

This concept, as previously mentioned, can be expressed writing an equation in integral and conservative form considering a fixed and finite control volume (1.2).

$$\frac{\partial}{\partial t}\int_V \rho dV + \int_S \rho \boldsymbol{V}\cdot\boldsymbol{n}dS = 0 \tag{1.2}$$

1.2.2 Momentum balance equation

The physical principle expressed is Newton's second law (1.3). This is a vector equation since the force $\boldsymbol{F}$ and the velocity $\boldsymbol{V}$ are vectors.

$$\boldsymbol{F} = \frac{d(m\boldsymbol{V})}{dt} \tag{1.3}$$

In this case we obtain three equations, corresponding to the projection in the three Cartesian directions:

$$\frac{\partial}{\partial t}\int_V \rho u dV + \int_S \rho u \boldsymbol{V}\cdot\boldsymbol{n}dS + \int_S p n_x dS = \int_S \tau_x\cdot\boldsymbol{n}dS + \int_V \rho f_x dV \tag{1.4}$$

$$\frac{\partial}{\partial t}\int_V \rho v dV + \int_S \rho v \boldsymbol{V}\cdot\boldsymbol{n}dS + \int_S p n_y dS = \int_S \tau_y\cdot\boldsymbol{n}dS + \int_V \rho f_y dV \tag{1.5}$$

$$\frac{\partial}{\partial t}\int_V \rho w dV + \int_S \rho w \boldsymbol{V}\cdot\boldsymbol{n}dS + \int_S p n_z dS = \int_S \tau_z\cdot\boldsymbol{n}dS + \int_V \rho f_z dV \tag{1.6}$$

These equations are three scalar equations for the components of a vector quantity and can be written in a compact form as a single vector equation (1.7):

$$\frac{\partial}{\partial t}\int_V \rho \boldsymbol{V} dV + \int_S \rho \boldsymbol{V}\boldsymbol{V}\cdot \boldsymbol{n} dS + \int_S p\bar{I}\cdot \boldsymbol{n} dS = \int_S \bar{\tau}\cdot \boldsymbol{n} dS + \int_V \rho \boldsymbol{f} dV \tag{1.7}$$

In these equations we can see the presence of volumetric forces and surface forces. Volumetric ones act at a distance directly on the mass contained in the control volume, an example is the gravitational force. In this case they are represented by the vector $\boldsymbol{f}$. Surface ones act directly on the surface of the control volume and they are represented by the pressure p and the shear and normal stresses expressed by $\bar{\tau}$.

The momentum balance equation is particularly important in this document because is the fundamental idea the far-field methods analyzed are based on .

1.2.3 Energy balance equation

The energy is conserved is the physical principle expressed by the First Principle of Thermodynamics. It can be applied to the control volume and we obtain that the sum of the net flux towards the control volume and the work done per unit time on the control volume by volumetric and surface forces equals the rate of change of the total energy in the control volume.

In the integral conservative form the energy balance equation is (1.8):

$$\int_V \frac{\partial E}{\partial t} dV + \int_S (E+p)\boldsymbol{V}\cdot \boldsymbol{n} dS - \int_S (\bar{\tau}\cdot \boldsymbol{V})\cdot \boldsymbol{n} dS + \int_S \dot{\boldsymbol{q}}\cdot \boldsymbol{n} dS = \int_V \rho \dot{\xi} dV + \int_V \rho \boldsymbol{f}\cdot \boldsymbol{V} dV \tag{1.8}$$

E is the total energy per unit volume, $\dot{\boldsymbol{q}}$ is the heat flux due to thermal conduction and can be written through Fourier's Law (1.9), $\dot{\xi}$ is the heat absorbed per unit time and unit mass.

$$\dot{\boldsymbol{q}} = -k\nabla T \tag{1.9}$$

1.2.4 Notes

Depending on the cases, it can be useful to use Gauss' Theorem to transform the surface integral of fluxes in the volume integral of the divergence. For a generic quantity $\boldsymbol{g}$:

$$\int_S \boldsymbol{g}\cdot \boldsymbol{n} dS = \int_V \nabla\cdot \boldsymbol{g} dV \tag{1.10}$$

Another important consideration to be made is the fact that the governing equations of fluid dynamics are a non-linear system of partial equations and in general a closed form does not exist.

As we have just seen there are five governing equations of fluid dynamics, one for mass balance, three for the momentum balance and one for the energy balance. However the number of unknowns is seven, so in order to close the system two more equations are needed. In typical aerodynamics application we can consider the gas as a perfect gas, meaning that the perfect gas law can be used

(1.11). Moreover for a perfect gas the specific heats are constant, so that the seventh equation is represented by (1.12).

$$p = \rho R^* T \tag{1.11}$$

$$e = C_v T \tag{1.12}$$

As will be discussed in the following chapters, this consideration will be useful. In this way is possible to work with an acceptable approximation without compromising the accuracy of the results shown.

Chapter 2

Presentation of the far-field methods

The philosophy of the far-field methods was inspired by Theodore Von Kármán. His idea was to apply the conservation laws to a control volume surrounding the body of interest, in this way the key point, as mentioned in the previous chapter, is the fact that the forces applied on the skin of the body can be calculate not from an integration on the body skin itself but rather integrating directly in the flow domain. This can lead to a drag breakdown in viscous, wave and lift-induced drag, which means that the drag can be decomposed into its phenomenological sources.

The sum of viscous and wave drag is defined as profile drag D_{vw}, also defined as irreversible drag. This is useful since the first formulations do not take into account to compute the lift-induce drag, which is approximated using formulas based on elliptic loading and aspect ratio.

The far-field methods can be grouped in two families, depending on the formulations: thermodynamic formulations and vortical formulation. The former evaluate the aerodynamic forces from the measurement of thermodynamic quantities such as entropy, pressure, temperature and total enthalpy, whereas the latter evaluate the aerodynamic forces through velocity and vorticity vectors.

This document will focus the attention on thermodynamic ones but a brief presentation of vortical ones will be presented.

2.1 Thermodynamic formulations

The thermodynamic breakdown of drag has first been developed for steady flows. Usually for steady flows all far-field decompositions start from the same momentum balance in a control volume Ω bounded by a closed surface S_e. For convenience, as we will see later, the plane behind the body, i. e. in its wake, is defined as wake plane S_w (fig. 2.1).

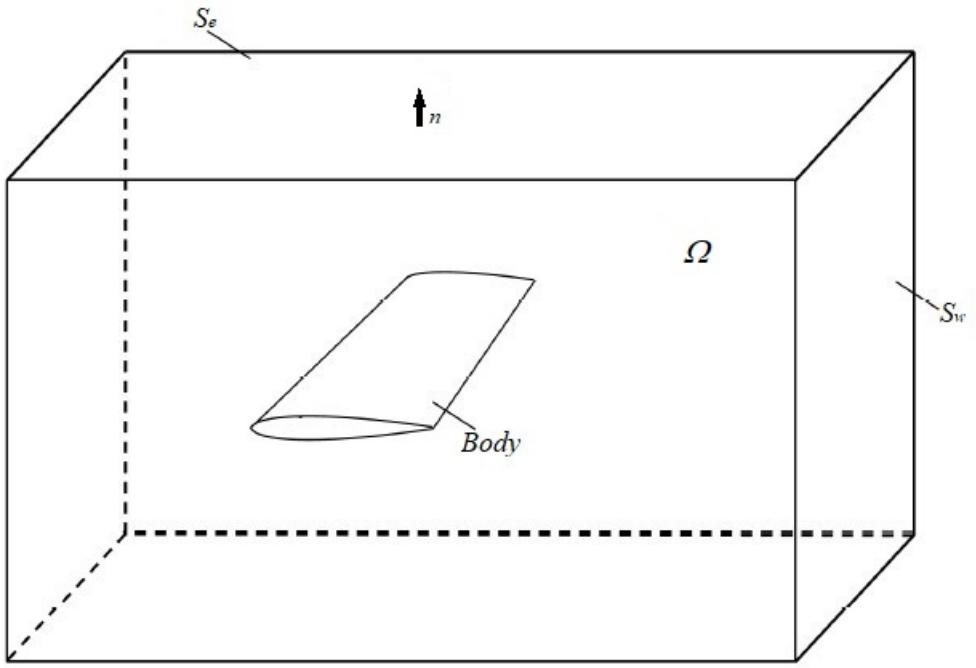

Figure 2.1: Control volume (modified from [8])

Within the thermodynamic formulations there is a distinction between the pressure-based formulations and the entropy-based formulations. However this approach are very similar and the main difference is the different choice of the variables.

2.1.1 Betz's formulation

In 1925 Betz [1] has been one of the first to propose a formulation for the evaluation of the profile drag, valid for incompressible flows.

As stated previously, induced drag was computed from approximated formulas taking into account elliptic loading and aspect ratio. The profile drag was then obtained as the difference between the total drag and the induced drag, clearly lacking accuracy. The idea of Betz is then to compute the profile drag from the wake produced by the aircraft, using experimental measurements with a bent or a Pitot tube placed in the wake of the wing or aircraft. In his document Betz explains that

in order to better understand the idea, a simpler case without the presence of lift is considered. However the final result is valid also for a lift-producing body.

He assumes that the streamlines of the flow in a wake plane S_w downstream the body are aligned with the free stream ones and that the variations of stagnation temperature are negligible, obtaining:

- $v = w = 0$
- $T_0 = T_{0_\infty}$

The resulting final formula to compute the profile drag is then:

$$D_{vw} = \int_{S_w} (p_{0_\infty} - p_0) dS - \frac{\rho}{2} \int_{S_w} (u' - u)(2u_\infty - u' - u) dS \tag{2.1}$$

In this equation p_0 is the total pressure $p + 1/2\rho u^2$, $p_{0\infty}$ is the total pressure upstream the body, u_∞ is the velocity of the free stream and u' is the velocity of a potential flow which would be identical to the real flow outside the vortical region, which means that the second integral is limited to the vortical region. Betz admits that the second integral is difficult to compute and through an analysis of the order of magnitude he shows that the second integral is less than 1/20 of the first one and can be neglected for preliminary analysis [1].

2.1.2 Jones' formulation

The idea of Jones is basically the same expressed by Betz but with more restrictive hypotheses, considering to use a Pitot tube for the measurements in the wake. In this way the aim is to get rid of the second integral of Betz's formula [3].

He assumes that on the wake plane S_w the static pressure is equal to the reference static pressure, and that the velocity is aligned with the free stream velocity:

- $p = p_\infty$
- $v = w = 0$

The final resulting formula is:

$$D_{vw} = p_{d_\infty} \int_{S_w} 2\sqrt{p_d^* - p^*}(1 - \sqrt{p_d^*}) dS \tag{2.2}$$

with p_d the dynamic pressure $1/2\rho u^2 = p_0 - p$, $p_d^* = p_d / p_{d_\infty}$ and $p^* = p/p_\infty$ the dimensionless dynamic pressure and static pressure.

This formulation depends only on dynamic and static pressure for the estimation of the profile drag.

It has to be noted that now the surface S_w can be limited to the wake boundary of the stream-tube enclosing the body, the boundary layer and the wake. Jones explains that in this way the plane of integration can be moved close to the trailing edge of the body, from section AA to section BB (fig. 2.2) and that the formulation does not depend on the location of the plane with the exception of what he called *dead zones*, i. e. regions where p_d^* is negative and as a consequence the

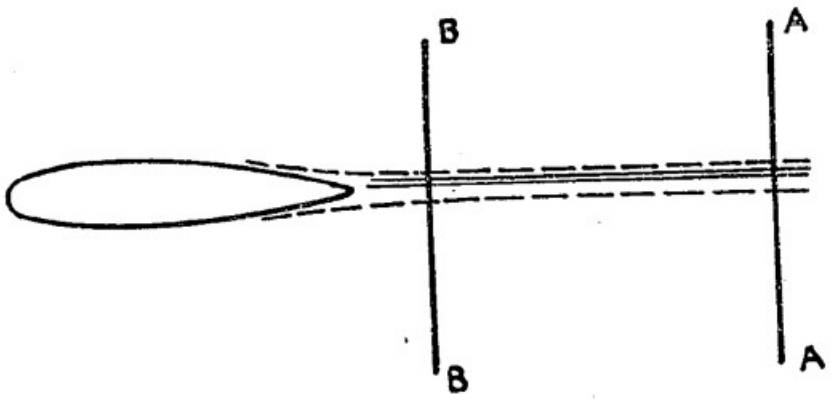

Figure 2.2: Different plane position according to Jones' formulation (from [3])

formulation is not defined.

A comparison between Jones' profile drag and Betz's one can be observed in (fig. 2.3).

2.1.3 Oswatitsch's entropy drag formulation

In 1956 Oswatitsch [5] developed a formulation which differs from the previous ones by its nature. Oswatitsch makes thermodynamic considerations instead of assuming transverse velocity equal to zero. In this way he expresses velocity and pressure as a function of the thermodynamic variables total enthalpy H and entropy s. The formula is derived from a momentum balance on a control surface taken far from the body and assuming an isenthalpic flow. In the wake:

- $H = H_\infty$
- $V \simeq U_\infty$

where $H = h + V^2/2$ is the total specific enthaply in the wake, $H_\infty = h_\infty + U_\infty^2/2$ is the freestream total specific enthaply.
Neglecting second orders terms, with isenthalpic flow, the formula for the profile drag is:

$$D_{vw} = \frac{T_\infty}{u_\infty} \int_{S_w} \rho u \Delta s dS \tag{2.3}$$

with $\Delta s = s - s_\infty$ the increment in specific entropy.

Thanks to this definition it is possible to avoid restrictive hypotheses in the wake plane. It is possible to demonstrate that this three formulation are equivalent at first order, as shown by Métheut in his Ph.D Thesis [4].

2.1.4 Paparone and Tognaccini's formulation

In 2003 Paparone and Tognaccini proposed a formulation thanks to which it is possible to decompose the total drag into the three contribuitions of lift-induced drag, viscous drag and wave drag [6].

They considered S_e far enough from the body in such way that

- $\boldsymbol{\tau} \cdot \boldsymbol{n} \simeq 0$
- $\Delta p/p_\infty, \Delta s/R, \Delta H/U_\infty^2 << 1$ where $\Delta p = p - p_\infty$ and $\Delta H = H - H_\infty$

The drag formula, which holds for a perfect gas, is:

$$D = \oint_{S_e} \left(\rho_\infty U_\infty^2 \frac{1}{\gamma M_\infty^2} \frac{\Delta p}{p_\infty} n_x + U_\infty f\left(\frac{\Delta p}{p_\infty}, \frac{\Delta s}{R}, \frac{\Delta H}{U_\infty^2} \right) \rho (\boldsymbol{V} \cdot \boldsymbol{n}) \boldsymbol{i} \right) dS \tag{2.4}$$

with

$$f\left(\frac{\Delta p}{p_\infty}, \frac{\Delta s}{R}, \frac{\Delta H}{U_\infty^2} \right) = \sqrt{1 + \frac{2\Delta H}{U_\infty^2} - \frac{2}{(\gamma - 1) M_\infty^2} \left(\left(\left(1 + \frac{\Delta p}{p_\infty} \right) e^{\Delta s/R} \right)^{(\gamma-1)/\gamma} - 1 \right)} \tag{2.5}$$

The profile drag definition is based on the entropy drag and can be expressed with a volume integral upon applying the divergence theorem:

$$D_{vw} = U_\infty \int_\Omega \nabla \cdot \left(\rho g \left(\frac{\Delta s}{R} \right) \boldsymbol{V} \right) dV \tag{2.6}$$

with

$$g\left(\frac{\Delta s}{R} \right) = \frac{1}{\gamma M_\infty^2} \frac{\Delta s}{R} + \frac{1 + (\gamma - 1) M_\infty^2}{2\gamma^2 M_\infty^4} \left(\frac{\Delta s}{R} \right)^2 \tag{2.7}$$

The volume can be splitted in two different regions, the boundary layer region Ω_v and the shock wave region Ω_w, in such way to decompose the profile drag into its contributions of viscous and wave drag. The two different drag contributions are:

$$D_v = U_\infty \int_{\Omega_v} \nabla \cdot \left(\rho g \left(\frac{\Delta s}{R} \right) \boldsymbol{V} \right) dV \tag{2.8}$$

$$D_w = U_\infty \int_{\Omega_w} \nabla \cdot \left(\rho g \left(\frac{\Delta s}{R} \right) \boldsymbol{V} \right) dV \tag{2.9}$$

It can be then noticed that the integrand for viscous and wave drag is the same, but in order to obtain the different contributions it is important to consider the correct region of integration.

2.1.5 Destarac and Van der Vooren's formulation

Van der Vooren has been the first to perform a thermodynamic breakdown of the far-field drag in 1990 [11] and his method consists in a sort of crossover between the hypotheses on a wake plane and the thermodynamic consideration of Oswatitsch.

The main aspect of Van der Vooren's formulation is the breakdown of profile drag into its components of viscous and wave drag. However, initially this formulation has not been directly applied to industrial cases because the lack of accuracy between far-field and near-field values. In 1993 Destarac solved this issue with a formalization of the concept of *spurious drag*.

The formulation here presented is the one for non-propelled aircraft. It starts from the far-field equation obtained applying the conservation of mass and momentum in a control volume Ω (fig. 2.4). The upstream and lateral surfaces are chosen at infinity in such way the integration limits to the downstream surface S_w, i. e. the one in the wake.

The idea is to assume a flow free from vortices, which means that the profile drag is the only one to be exerted on the body. Under this considerations, on a plane S_w far enough from the sources of drag:

- $\boldsymbol{\tau_x} = 0$
- $v = w = 0$
- $p = p_\infty$

With these assumptions, the key point is now to express the axial velocity defect $u - u_\infty$ (later in this document, based on the work done by H. Toubin [8] this difference will be expressed as $\Delta u = u_{irr} - u_\infty$). We obtain:

$$\Delta u = u_\infty \sqrt{1 + \frac{2\Delta H}{u_\infty^2} - \frac{2}{(\gamma-1)M_\infty^2}\left(e^{\frac{\gamma-1}{\gamma}\frac{\Delta s}{R}} - 1\right)} - u_\infty \tag{2.10}$$

In case of flow free from vortices, under this assumptions, the total drag is equal to the profile drag:

$$D = D_{vw} = -\int_{S_w} \rho \Delta u (\boldsymbol{V} \cdot \boldsymbol{n}) dS \tag{2.11}$$

The final operation is then to extract from the profile drag the contributions of viscous and wave drag. To do so, the wake surface integral is transformed into a volume integral using the divergence theorem and considering a truly inviscid flow outside Ω_v and Ω_w. As previously seen before for Paparone and Tognaccini's formulation, the integrands are the same, the volume of integration are the ones which determines the two different contributions. The final formulas are:

$$D_v = -\int_{\Omega_v} \nabla \cdot (\rho \Delta u \boldsymbol{V}) dV \tag{2.12}$$

$$D_w = -\int_{\Omega_w} \nabla \cdot (\rho \Delta u \boldsymbol{V}) dV \tag{2.13}$$

The induced drag can then be computed as the complementary part, which can also be written as volume term:

$$D_i = -\int_{\Omega_v \cup \Omega_w} \nabla \cdot (\rho(u - u_\infty - \Delta u)\boldsymbol{V} + (p - p_\infty)\boldsymbol{i} - \boldsymbol{\tau_x})dV - D_p - D_f \tag{2.14}$$

where D_p is the pressure drag and D_f is the friction drag, both coming from the near-field drag integration.

We can write the notation $\boldsymbol{f} = \rho(u - u_\infty - \Delta u)\boldsymbol{V} + (p - p_\infty)\boldsymbol{i} - \boldsymbol{\tau_x}$ and this vector has the property

$$\nabla \cdot \boldsymbol{f} = 0 \tag{2.15}$$

Spurious drag concept

Theoretically the balance between near-field drag and far-field drag is established. In reality the values obtained from the far-field drag computation always differ from the near-field ones and this concept has been formalized as *spurious drag*.

The causes of this numerical deviations can be:

- a spurious contribution of $\nabla \cdot (\rho \Delta u \boldsymbol{V})$ in the near field outside $\Omega_v \cup \Omega_w$ due to the artificial creation of entropy
- the numerical and physical dissipation caused by the trailing vortices outside $\Omega_v \cup \Omega_w$

As we will analyze later in the document, in the application of far-field methodologies to a commercial CFD software, the presence of this spurious drag is always present and the weight of its importance can differs depending on the type of analysis conducted, the physics of the flow taken into account, the different mesh realization of the domain, the different boundary condition.

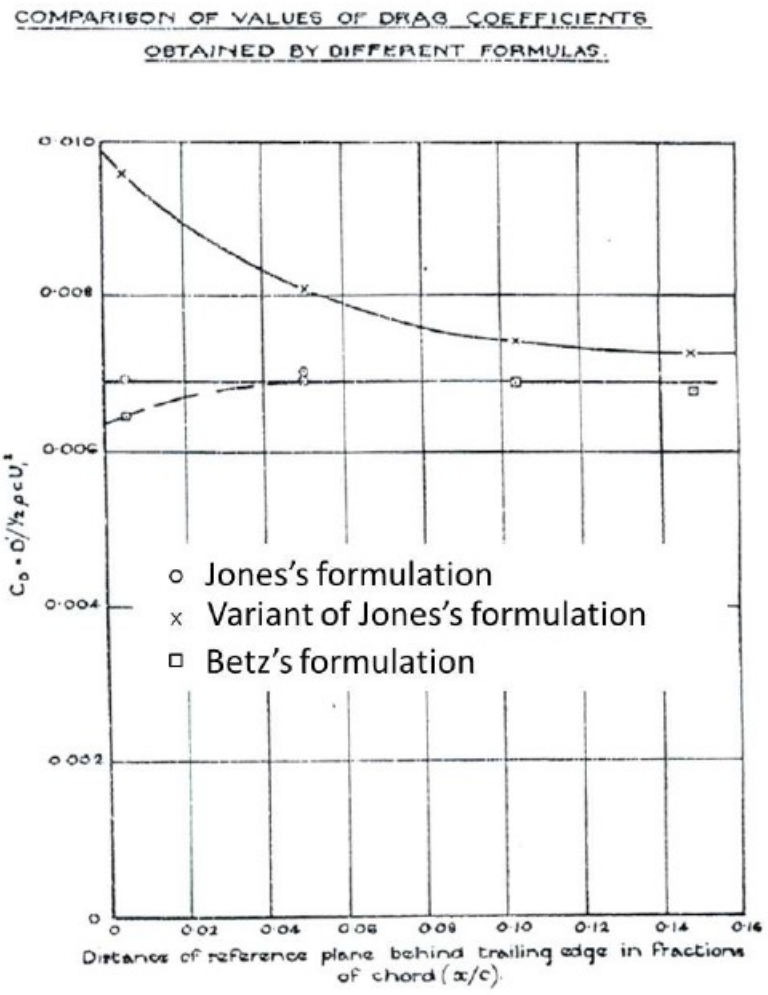

Figure 2.3: Comparison between two different variations of Jones' formulation and Betz's formulation (from [3])

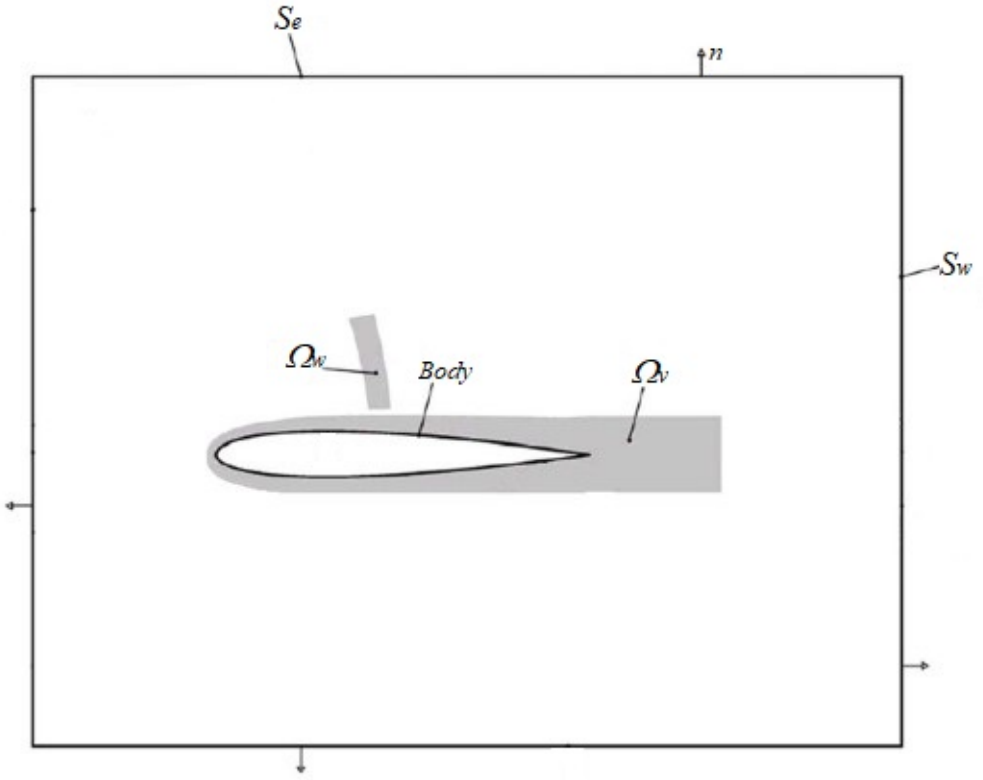

Figure 2.4: Control volume defined by Destarac and Van der Vooren (modified from [10])

2.2 Vortical formulations

The vortical formulations differ from the thermodynamic ones because they focus the attention on the velocity and vorticity vectors rather than thermodynamic quantities. Since this document will focus the attention on thermodynamic formulations, here a brief presentation of vortical ones is shown for theoretical completeness of far-field methodologies.

Between the vortical formulations, a distinction can be made: the circulation-based and the vorticity-based.

The circulation-based formulations evaluate the aerodynamic force from the circulation produced by the wings. The vorticity-based ones link the aerodynamic force to the velocity and vorticity vectors. The latter are more recent and usually they can be applied to more complex flow conditions. Among the most important authors who worked on this formulations we remember Kutta, Joukowski, Filon, Prantdl, Saffman, Maskell, more recently Wu.

An important formula belonging to the vortical ones is the one represented by the so-called Lamb-Vector, defined as the cross-product between velocity vector and vorticity vector:

$$\boldsymbol{l} = \boldsymbol{V} \times \boldsymbol{\omega} \tag{2.16}$$

The total force acted on the body is expressed in terms of vortex force. Saffman used the hypothesis of inviscid flow, already used by Prandtl. Thanks to the work of Wu the formulations has been extended to viscous flow, where pressure is eliminated from the final formula.

Van der Vooren and Destarac's formulation have been proved to be accurate, but the use of vortical formulations and Lamb-Vector one can be useful in case of analysis of lift and lift-induced drag, since they are better suited for the study of vortices and complex flows in general.

Chapter 3

CFD software presentation and near-field drag analysis

The objective of this Thesis is to implement in a commercial CFD software the far-field methods and see their accuracy and how they can be used to predict the different drag contributions. To do so, the software for CFD simulation *STAR-CCM+* has been used, provided by the company *Siemens* [7].

This chapter will present what is a CFD software and why it is now widely used in a great range of engineering applications (fig. 3.1). Then we will see how a simulation is performed describing all the characteristics involved and we will study the near-field drag analyzing the mesh-grid independence concept and explaining why it is important.

3.1 Computational Fluid Dynamics simulation

As already presented in the first chapter, the Computational Fluid Dynamics (CFD) is a powerful numerical tool which can be used to perform 2D and 3D steady and unsteady simulations of the fluid motion.

The reasons why in the last decades the use of this instrument has increased are different. Compared to experimental analysis, CFD ones are less expensive, faster to perform, allow the study of phenomena difficult to analyze in physical experiment. From what it has been just said it may look that the use of CFD can replace the experimental analysis but in reality they have to be used together and compare them to see possible discrepancies between the two approaches, in fact it is always important to verify the results obtained through experimental validations. As we will see later, the use of CFD implies various issues, since the accuracy depends on the fidelity of the model, the approximations and assumptions involved in the simulation.

CFD simulations are based on the Navier-Stokes equations, used to described the quantity involved in the fluid motion such as temperature, density, pressure, velocity and others. The main aspect involved in a simulation is how these equations are used to mathematically formulate the physical problem and the numerical methods used to resolve the equations. The results obtained

will clearly be an approximation of the reality but the key point is to make the right assumptions in order to minimize the errors and reach an acceptable accuracy and here is where the experimental validation is involved.

A CFD simulation follows these three generalized steps:

- preprocessing
- solving
- postprocessing

The preprocessing step consists in the creation of a 2D/3D geometry of interest and breaking up the domain into volumes/cells in a process called meshing or grid generation. Here is where all the conditions and variables are translated into mathematical models and equations.

The solving step is the one which typically requires the majority of time and computing resources, because it is the stage where the CFD software resolves iteratively the discretized equations.

The postprocessing is the last step and it is where, after the solving part is complete, the analysis and visualization of results can be performed with reports, monitors and plots.

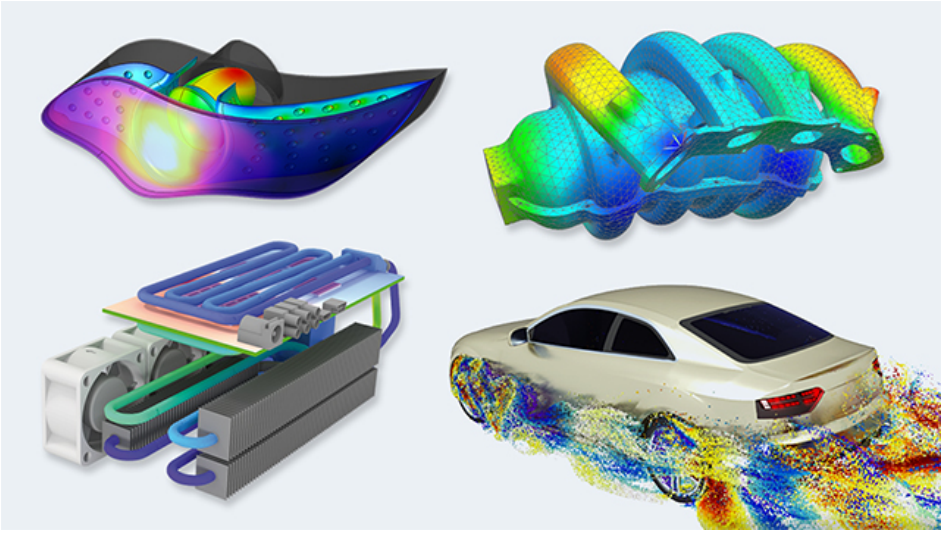

Figure 3.1: Typical engineering applications where CFD software is used (from [7])

3.2 2D simulation and near-field drag analysis

In this section a 2D simulation is presented and all the aspects are described. Different mesh will be presented and we will analyze the near-field drag and grid independence concept.

The simulation is conducted on the NACA0012 airfoil with chord equal to $c = 1[m]$ at angle of attack $\alpha = 0°$. The static temperature is chosen at $T = 300[K]$, the number of Mach is set to $M = 0.8$ and the Reynolds number is $Re = 3 \cdot 10^6$. From the definition of the Reynolds number (3.1) it is possible to find the density (3.2) and since the gas is considered ideal, the reference pressure can be found from the equation for a perfect gas (1.11). The velocity is computed using the Mach number with the speed of sound definition (3.3).

$$Re = \frac{\rho V c}{\mu} \tag{3.1}$$

$$\rho = \frac{Re\mu}{Vc} \tag{3.2}$$

$$V = Ma = M\sqrt{\gamma RT} \tag{3.3}$$

The dynamic viscosity is μ in (3.1) and (3.2). Since the gas considered is air, in (3.3) the ratio of specific heats is $\gamma = 1.4$ and the specific gas constant is $R = 287.05[J/(kgK)]$.

The model used presents the following characteristics:

- two dimensional
- solution interpolation
- steady
- ideal gas
- coupled flow, coupled energy
- RANS (Reynolds-Averaged Navier-Stokes) equations
- turbulent with K-Omega turbulence (SST Menter)
- wall distance, all $y+$ wall treatment

3.2.1 Setup

We start by creating the geometry. The airfoil is created importing a curve described as a series of points which can be tabulated for example in *Excel*. In a sketch the domain is defined, shaping it in a sort of a bullet-form (fig. 3.2a), with extension of 200 chords upstream and downstream the airfoil. Although the simulation is two-dimensional, *STAR-CCM+* requires an extrusion of the sketch created and in a following step the simulation is defined as 2D. The computation is executed in the domain and in order to perform analysis on the airfoil, this is seen as an external obstacle in the domain. The final domain is than built by subtracting the airfoil from the bullet-shape of the sketch of the domain (fig. 3.2b).

After the creations of the geometry, this is divided into regions and we can create the mesh or grid. Here is where the creation of the 2D mesh is performed. Creating the grid means divide the domain into cells which can be of different shape depending on the mesher chosen, and in this way the RANS are applied to each cells and the resolution depends on the solver.

The mesher chosen is a polygonal one with prism layer. Different parameters can be modified from default or custom controls such as the base size, the target surface size, the prism layer total thickness and other controls.

The next step is to chose the model of the simulation and the main characteristics have been described in the previous page. Here other important choices of the simulation are presented. The coupled flow model has an implicit integration with *MUSCL 3rd-order/CD* discretization, the gradients presents a *Venkatakrishnan* limiter method, the solution interpolation uses a *Nearest neighbor* interpolation method, the wall distance method is *Implicit tree*, the SST (Menter) K-Omega has a 2nd-order convection. The AMG (Algebraic Multigrid) linear solver with *V-cycle* type is the one which is used.

Before running the simulation, the last step is to define the reference conditions, the initial and the boundary ones.

The reference static pressure is the one found with the perfect gas law (1.11), the initial conditions are represented by the static temperature $T = 300[K]$, the pressure is set $p = 0[Pa]$ because it is relative to the reference one, the velocity is the one obtained from (3.3).

The boundary conditions are defined in the *regions* section. The airfoil presents a *wall* type condition, the inlet has a *stagnation inlet* condition, with total pressure and total temperature computed from the isentropic formulas, the outlet condition is defined by a *pressure outlet* one, with pressure $p = 0[Pa]$ (always relative to the reference static one).

The simulation is ready to run.

Here we will focus the attention upon the creation of different grids depending on the controls previously described in the mesh creation and the number of total cells and we will see how the value of the near-field drag will change. All the others characteristics here described in the setup simulation are the same.

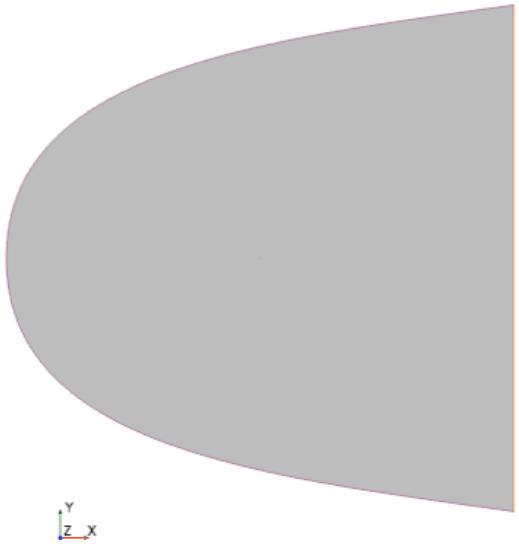

(a) Domain

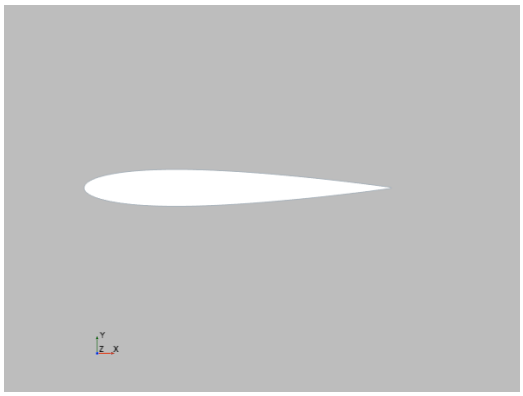

(b) NACA0012

Figure 3.2: Domain and airfoil of the simulation

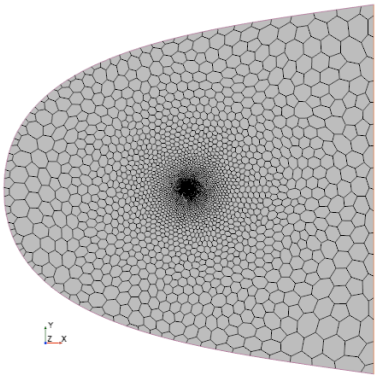

(a) Domain

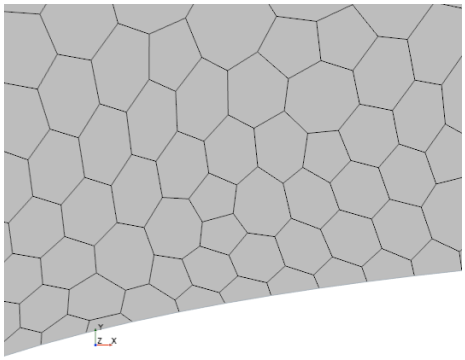

(b) Airfoil wall zoom

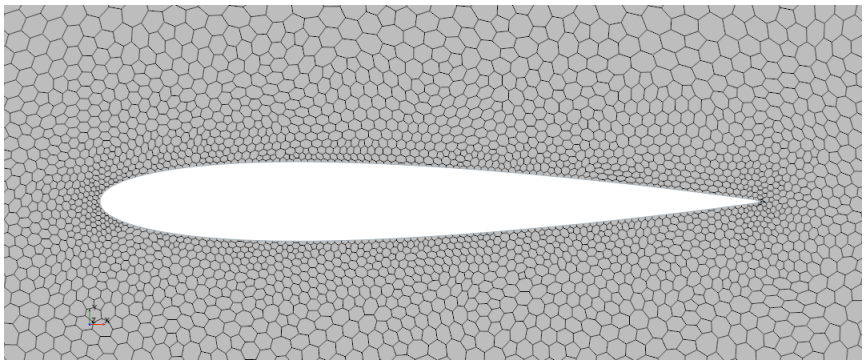

(c) Airfoil zoom

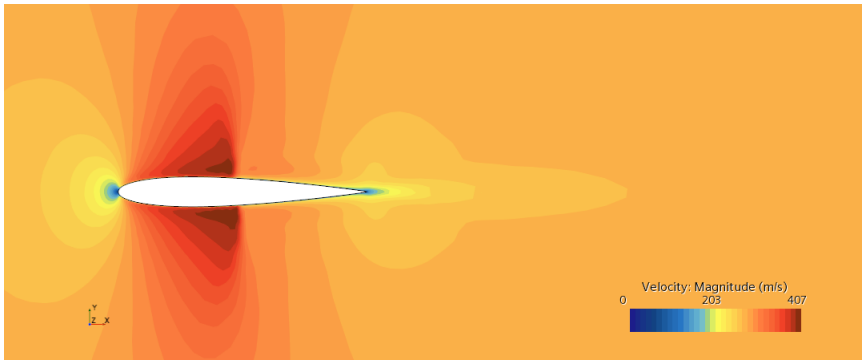

(d) Velocity magnitude scene

Figure 3.3: 8,111 cells grid simulation scenes

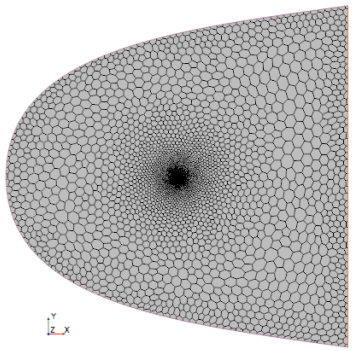

(a) Domain

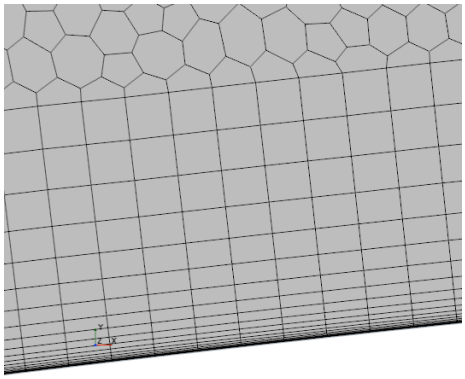

(b) Prism layer zoom

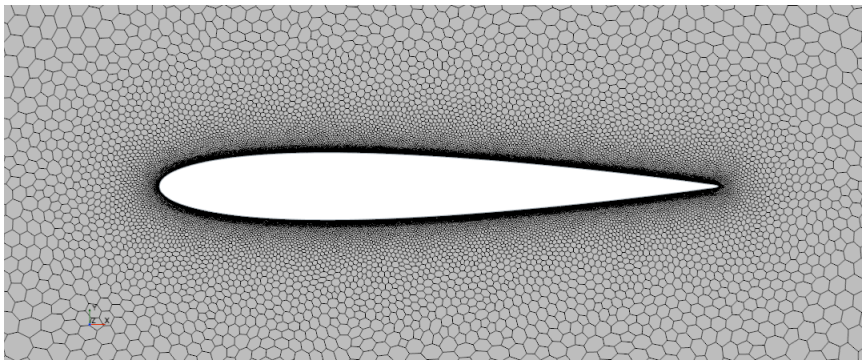

(c) Airfoil zoom

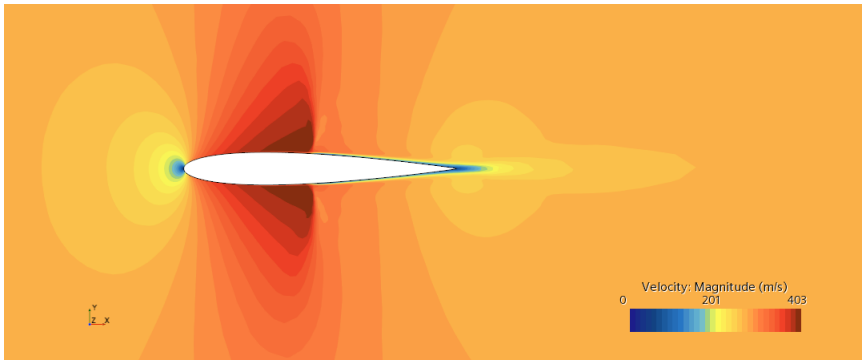

(d) Velocity magnitude scene

Figure 3.4: 53,844 cells grid simulation scenes

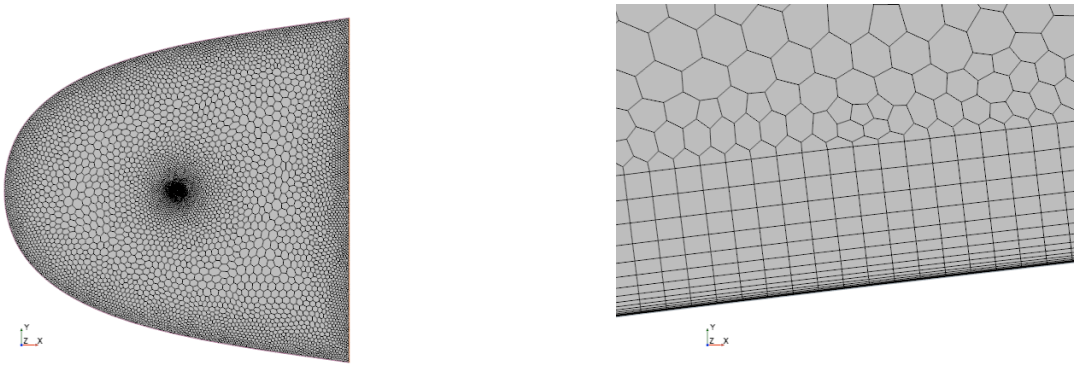

(a) Domain

(b) Prism layer zoom

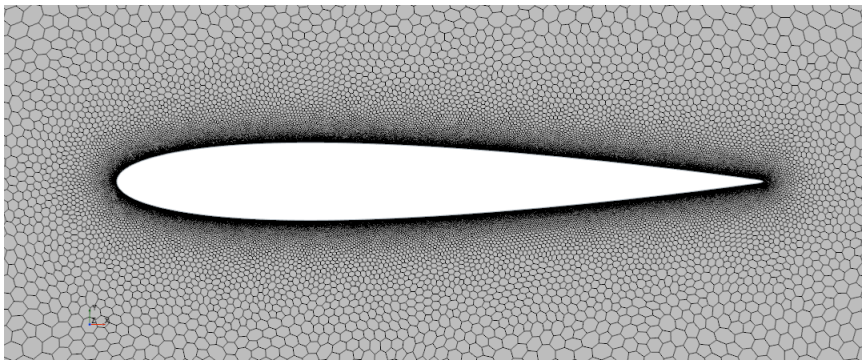

(c) Airfoil zoom

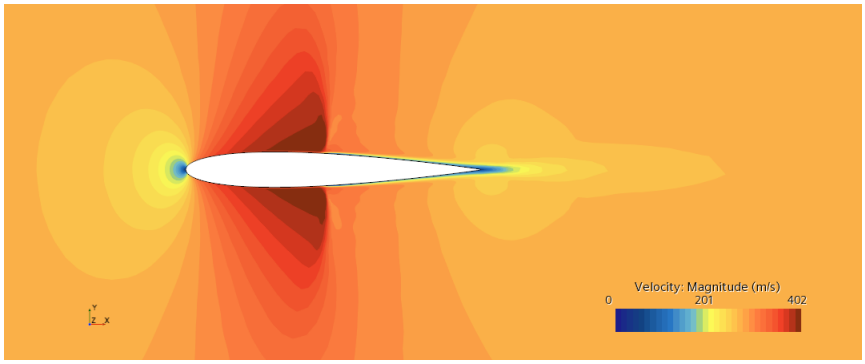

(d) Velocity magnitude scene

Figure 3.5: 132,434 cells grid simulation scenes

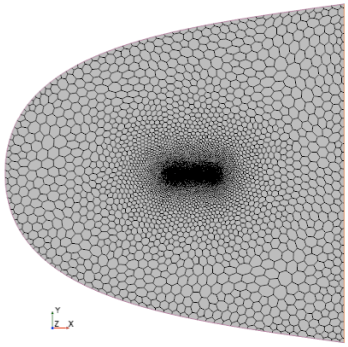

(a) Domain

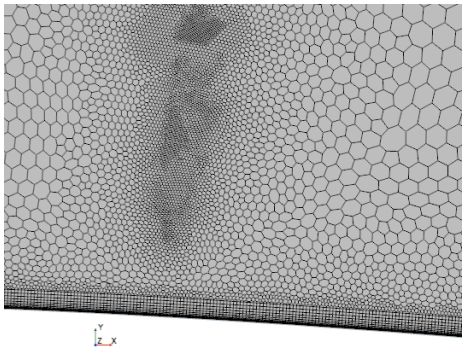

(b) Prism layer and shock refinement zoom

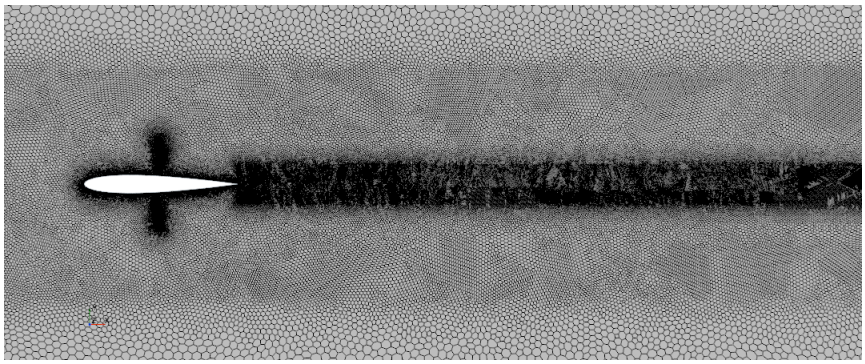

(c) Airfoil, shock and wake zoom

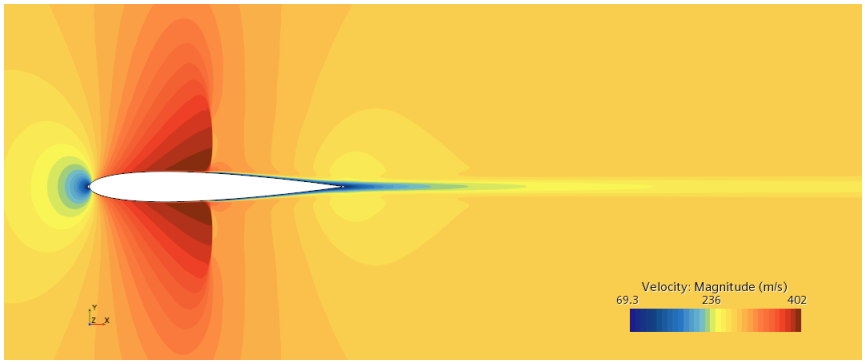

(d) Velocity magnitude scene

Figure 3.6: 252,097 cells grid with shock and wake refinement simulation scenes

3.2.2 Final results

After all the simulation have reached convergence, a compare between the results obtained can be made.

Through the residuals plots (as an example the one for the 53,884 cells grid is here reported (fig. 3.7)) the number of iterations needed for the convergence of the solution can be extracted.

The near-field drag is computed with the integration on the surface of pressure and shear and a distinction between the two contributions can be observed. The results are displayed with drag coefficients expressed in drag counts (tab. 3.1).

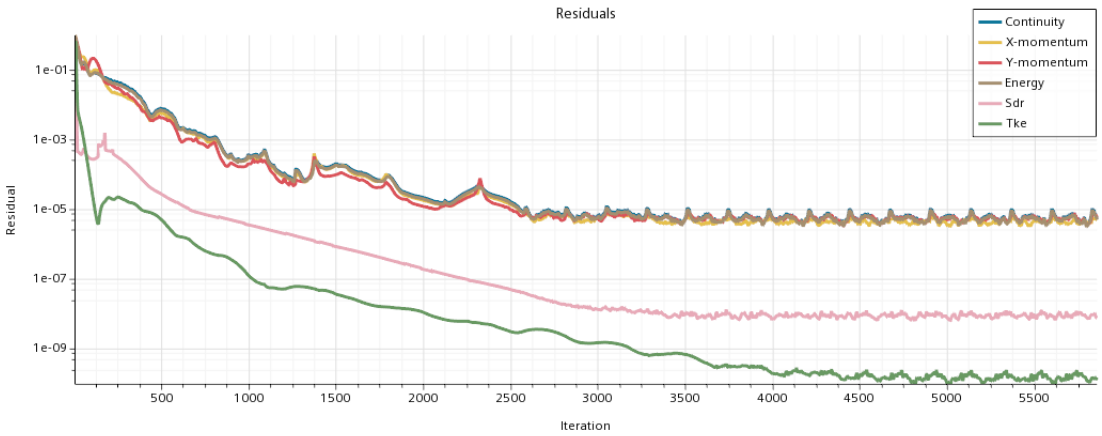

Figure 3.7: 53,884 cells grid residuals

	Iterations	*Drag [N]*	CD_{nf}	CD_{nf} *(press.)*	CD_{nf} *(shear)*
8,111 cells grid	$\simeq$ 2600	125.9739	176.2196	112.7752	63.4444
53,884 cells grid	$\simeq$ 4050	121.8841	170.4986	109.8911	60.6074
132,434 cells grid	$\simeq$ 4350	121.5574	170.0416	108.6046	61.4369
252,097 cells grid	$\simeq$ 5000	121.2773	169.6496	109.0789	60.5707

Table 3.1: Simulations results

From the final results it is clearly visible a convergence of values when the mesh realization is more and more fine. The coarse one presents values that differ quite a lot from the other grids, but this is understandable even from the fact that the boundary layer is not well captured since the prism layer is not present. Neglecting this one, the results obtained for the other three meshes are reaching a convergence with a difference than less than 1%. This explains the concept of grid independence which means that even if we try to realize a grid with more cells the values will change very little, so in a practical view this represents the fact that it is important to realize a sufficiently fine grid in order to obtain accurate results but also not so fine not to compromise time and computational resources.

The last important result to notice is the fact that the grid with 252,097 cells, despite the shock and wake refinements, produces near-field drag results really close to the ones without refinements. However this mesh will be analyze later in the document with the application of far-field drag methodologies where the analysis are conducted in the wake and close to the shock, so the difference between a non-refined grid and a refined one can produce big discrepancies in the results. It is clear that in case of far-field drag methods, as explained in the previous chapter, a fine grid in the wake is much more suited for the analysis.

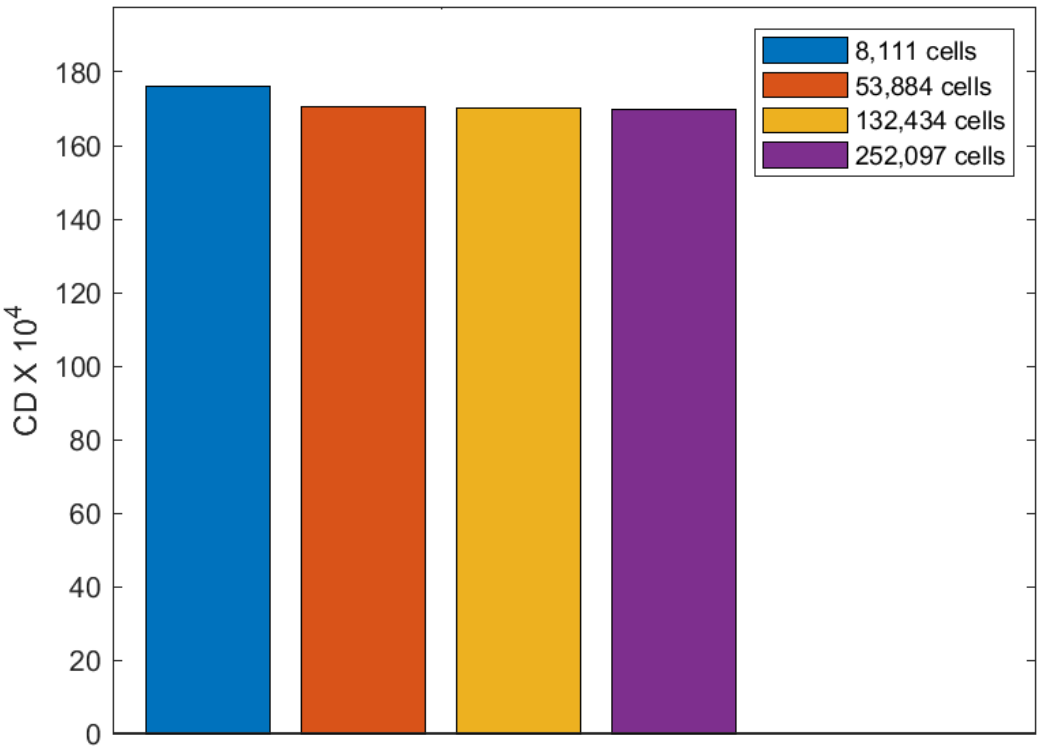

Figure 3.8: Comparison between CD_{nf}

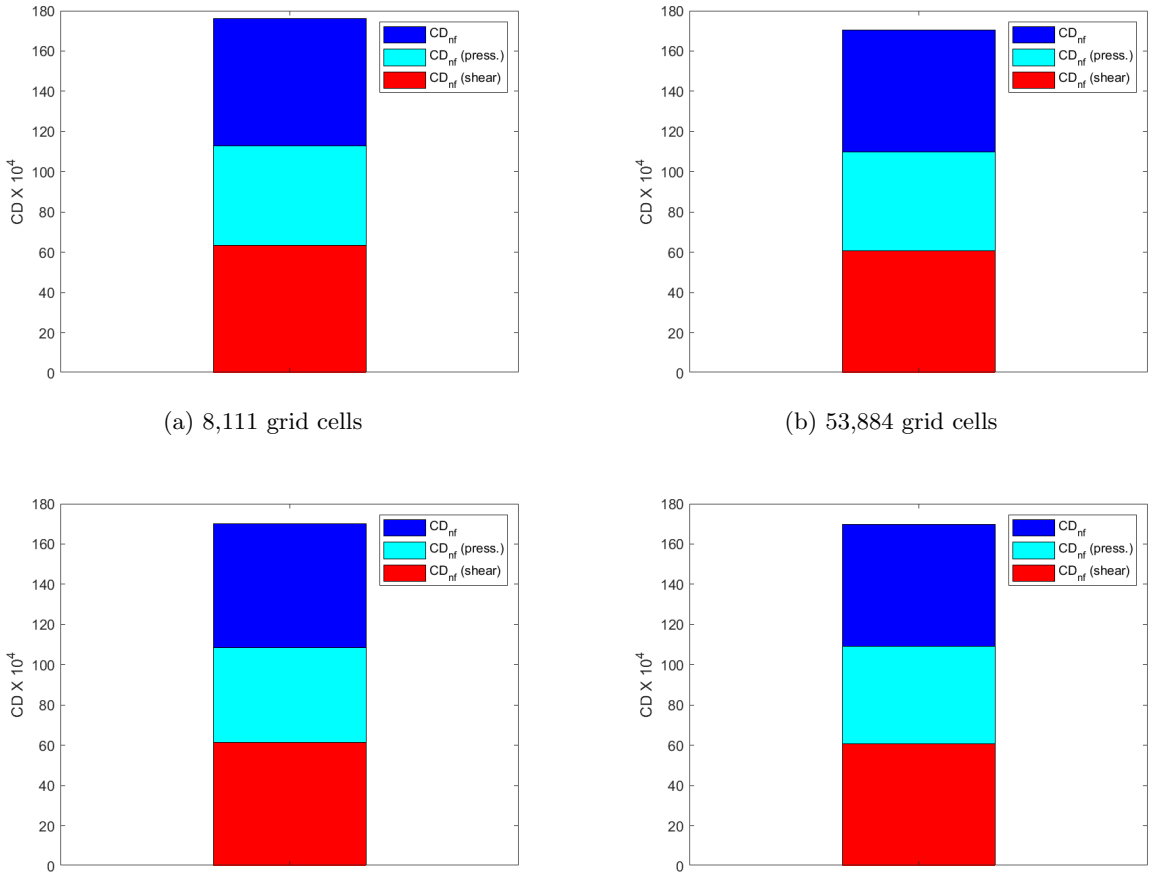

(a) 8,111 grid cells

(b) 53,884 grid cells

(c) 132,434 grid cells

(d) 252,097 grid cells

Figure 3.9: CD_{nf} with pressure and shear contributions for each grid

Chapter 4

Comparison between Betz's and Van der Vooren's formulations for total drag evaluation

In the previous chapter it has been described how a CFD commercial software works and how a simulation is conducted, followed by the analysis of the near-field drag. The aim here is to apply far-field methodologies and see how accurate the results of total drag obtained are in comparison to near-field drag. In the following chapters we will eventually focus on the far-field drag decomposition, analyzing 2D and 3D cases and extracting wave, viscous and induced drag.

4.1 2D simulation, steady case, $Mach = 0.15$, $Re = 6.5 \cdot 10^6$

In this section Betz's formulation and a generalized Van der Vooren's one for steady flows (based on the work done by H. Toubin [8]) will be applied to a subsonic 2D steady case with the NACA0012 airfoil.

Betz's formulation

We recall Betz's equation (2.1) for the computation of profile drag, which has been presented in chapter 2:

$$D_{vw} = \int_{S_w} (p_{0_\infty} - p_0) dS - \frac{\rho}{2} \int_{S_w} (u' - u)(2u_\infty - u' - u) dS \tag{4.1}$$

The analysis is conducted considering the complete formula and the first integral only in order to verify the orders of magnitude of the two integrals described in Betz's document [1].

New derivation of Van der Vooren's formulation

To derive the new formulation of Van der Vooren it has been considered the control volume in (fig. 2.1). We apply the conservation of mass and conservation of momentum and after some passages the drag is obtained by projecting the final vector equation along the free stream direction:

$$\int_{\partial\Omega} \rho(u-u_\infty)(\boldsymbol{V}\cdot\boldsymbol{n})dS + \int_{\partial\Omega}(p-p_\infty)(\boldsymbol{i}\cdot\boldsymbol{n})dS - \int_{\partial\Omega}(\boldsymbol{\tau_x}\cdot\boldsymbol{n})dS = 0 \tag{4.2}$$

The frontier of the domain $\partial\Omega$ is then split into the body surface S_{body} and the external surface S_e. The terms are rearranged, obtaining:

$$\int_{S_{body}} \left[(p-p_\infty)(\boldsymbol{i}\cdot\boldsymbol{n}) - (\boldsymbol{\tau_x}\cdot\boldsymbol{n})\right] dS = \int_{S_e} \left[-\rho(u-u_\infty)(\boldsymbol{V}\cdot\boldsymbol{n}) - (p-p_\infty)(\boldsymbol{i}\cdot\boldsymbol{n}) + (\boldsymbol{\tau_x}\cdot\boldsymbol{n})\right] dS \tag{4.3}$$

The left hand-side of (4.3) is the near-field drag and can broken down into pressure and friction drag:

$$D_p = \int_{S_{body}} (p-p_\infty)(\boldsymbol{i}\cdot\boldsymbol{n})dS \tag{4.4}$$

$$D_f = \int_{S_{body}} -(\boldsymbol{\tau_x}\cdot\boldsymbol{n})dS \tag{4.5}$$

$$D_{nf} = D_p + D_f \tag{4.6}$$

The right hand-side of (4.3) represents the far-field drag:

$$D_{ff} = \int_{S_e} (\boldsymbol{f}\cdot\boldsymbol{n})dS \tag{4.7}$$

where

$$\boldsymbol{f} = -\rho(u-u_\infty)\boldsymbol{V} - (p-p_\infty)\boldsymbol{i} + \boldsymbol{\tau_x} \tag{4.8}$$

We noticed that only classical fluid mechanics flow description assumptions have been made.

4.1.1 Simulation setup

Since Betz's formulation is valid for incompressible flows only, the case is set at Mach $M = 0.15$ in order to reduce at minimum air compressibility effects, condition which is in general satisfied for $M < 0.3$. Reynolds number is $Re = 6.5 \cdot 10^6$ and angle of attack $\alpha = 0°$.

All the characteristics of the model are the same described in the simulation (3.2). Here the main ones are reported:

- two dimensional
- solution interpolation
- steady
- ideal gas
- coupled flow, coupled energy
- RANS (Reynolds-Averaged Navier-Stokes) equations
- turbulent with K-Omega turbulence (SST Menter)
- wall distance, all $y+$ wall treatment

The ratio of specific heats is $\gamma = 1.4$ and the specific gas constant is $R = 287.05[J/(kgK)]$. The reference static pressure is computed from (1.11) and the initial conditions are static pressure $p = 0[Pa]$, static temperature $T = 300[K]$ and velocity found from (3.3).

The boundary conditions are:

- *wall* type for the airfoil
- *stagnation inlet*, with total pressure and temperature computed from the isentropic formulas
- *pressure outlet*

The domain extends for 200 chords upstream and downstream the airfoil. The mesh is realized using a polygonal mesher with prism layer and a refinement in the wake is made with the use of blocks and custom controls to define the desired tesselation (fig. 4.1c). The final grid has a total of 542,586 cells.

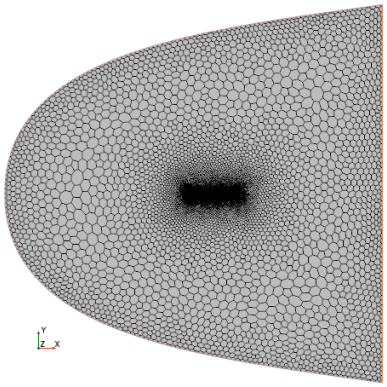

(a) Domain

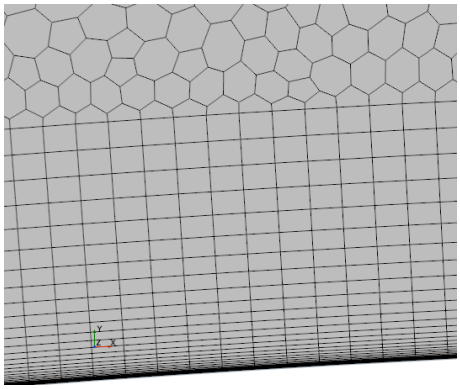

(b) Prism layer zoom

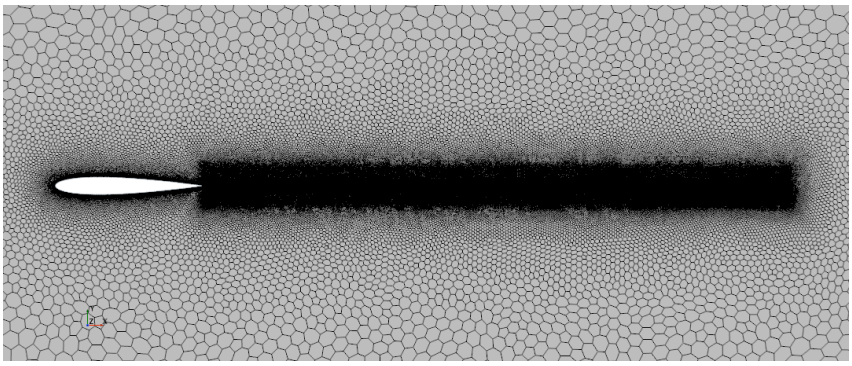

(c) Airfoil and wake refinement zoom

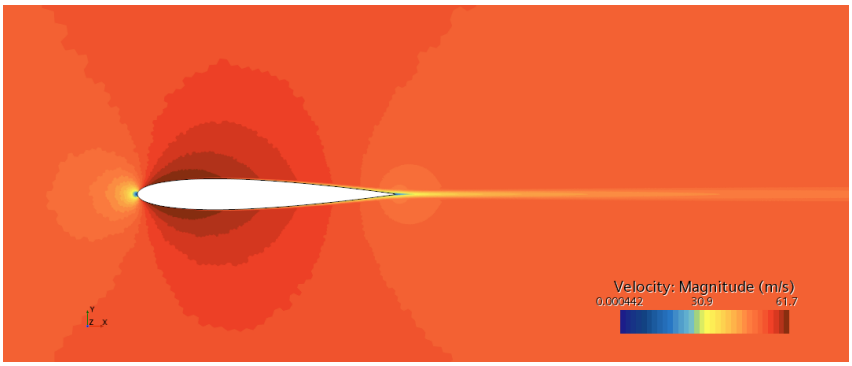

(d) Velocity magnitude scene

Figure 4.1: Simulation scenes

4.1.2 Post-processing and results

The convergence of the simulation is reached in around 1,020 iterations.

In order to analyze the far-field formulas, we create two field-functions, one for Betz's and one for the new derivation of Van der Vooren. The integrations are made on wake planes S_w positioned at different distance from the airfoil in terms of chords distance. These planes are created as *constrained planes* in the *derived parts* section of *STAR-CCM+* as shown in (fig. 4.2). As an example, in (fig. 4.3) it can be observed the convergence of the values of total drag force of the two formulation for each plane considered.

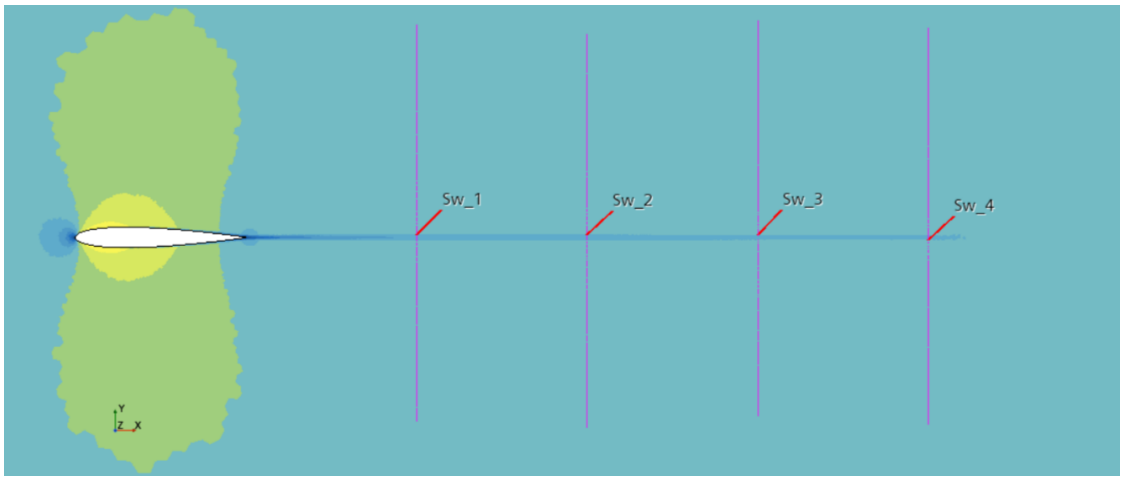

Figure 4.2: Wake planes where the integrations are performed

Given the assumptions and the parameters chosen, we assume that on the wake planes the term $\boldsymbol{\tau_x} \simeq 0$. As a consequence in the implementations of (4.7) this term is neglected and can be demonstrated that it is three orders of magnitude smaller than the others. Moreover the equation shows that the integration should be made consdering a surface which surrounds the airfoil but even in this case it can be demonstrated that the value coming from the integration on the wake plane represents the term with most weight, with 3/4 orders of magnitude greater than the values obtained from the integration on the lateral and upstream planes. As a result the integraton is made considering only the wake planes.

We obtain a near-field drag coefficient $CD_{nf} = 79.1625$ drag counts. In (fig. 4.4a) it is shown a comparison between the formulations and the near-field value: we observe a convergence of the results after about 3/4 chords, with the new formula of Van der Vooren more accurate than Betz's one if compared to the near-field drag coefficient with a difference in values of less than 0.5%. In (fig. 4.4b) and (fig. 4.5) it can be seen the comparison between the complete Betz's equation and considering only the first integral term: from the results it is confirmed that the second integral has an order of magnitude of less than 1/20 if compared to the first one, obtaining a difference of

about 1/30 in this case.

4.1.3 Comments

From the results obtained we can confirm the accuracy of the far-field drag formulations in terms of total drag. The new Van der Vooren's formulation presented here is the one which will be considered in the rest of the Thesis for the following analysis.

The verification of the implementation in a commercial CFD software of this formulas is already an important result but, as stated in the chapter 1, the advantage of far-field methodologies is the possibility of decomposing the drag into its phenomenological sources and this is the aim of the following chapters.

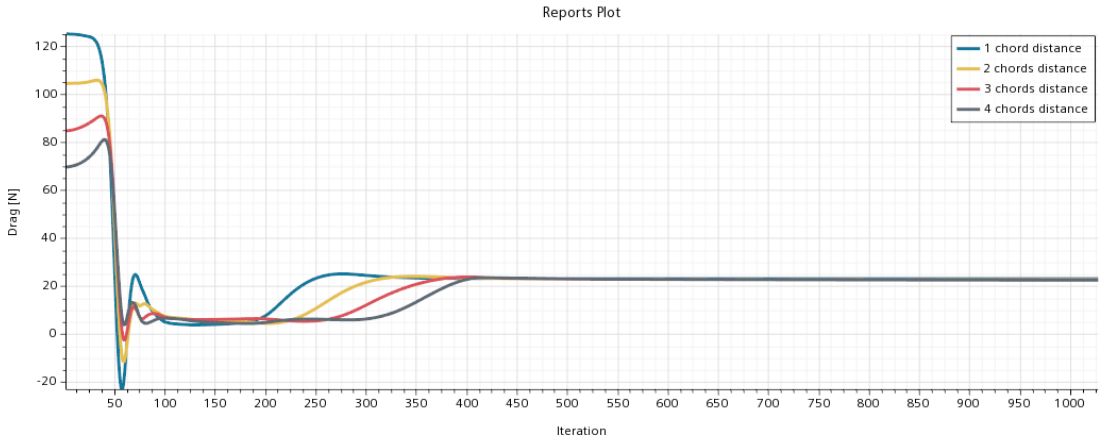

(a) Betz's formulation

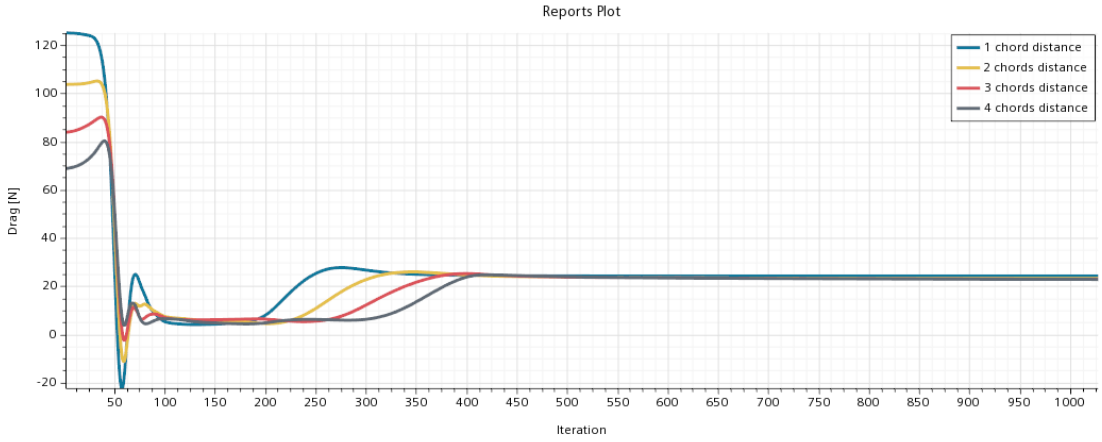

(b) New Var der Vooren's formulation

Figure 4.3: Convergence of total drag values for each formulation

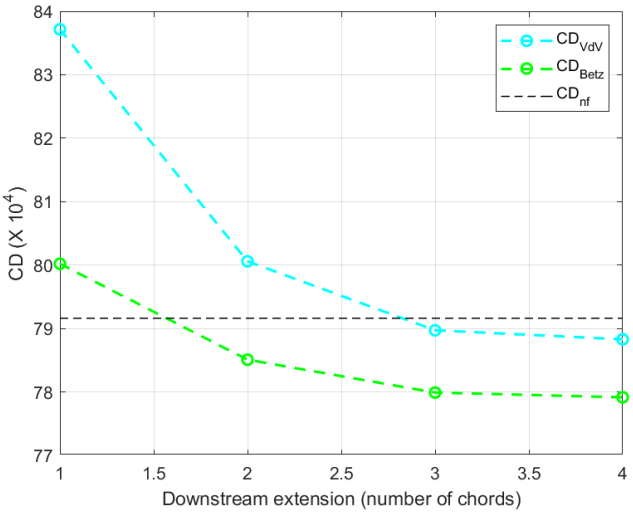

(a) Comparison between CD_{VdV}, CD_{Betz} and CD_{nf}

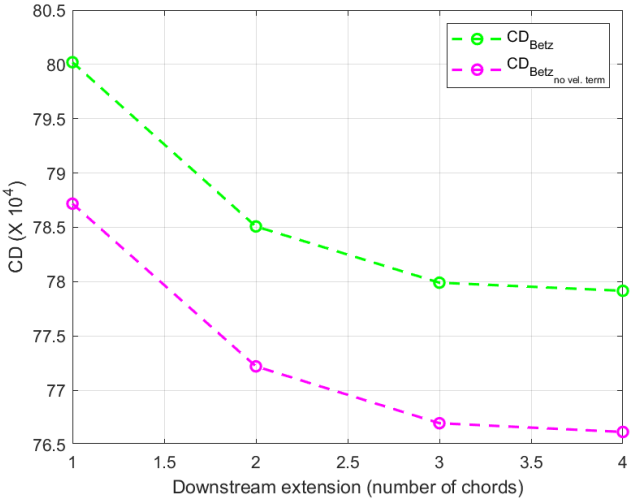

(b) Comparison between CD_{Betz} and CD_{Betz} neglecting the second integral in the formulation

Figure 4.4: Simulation results

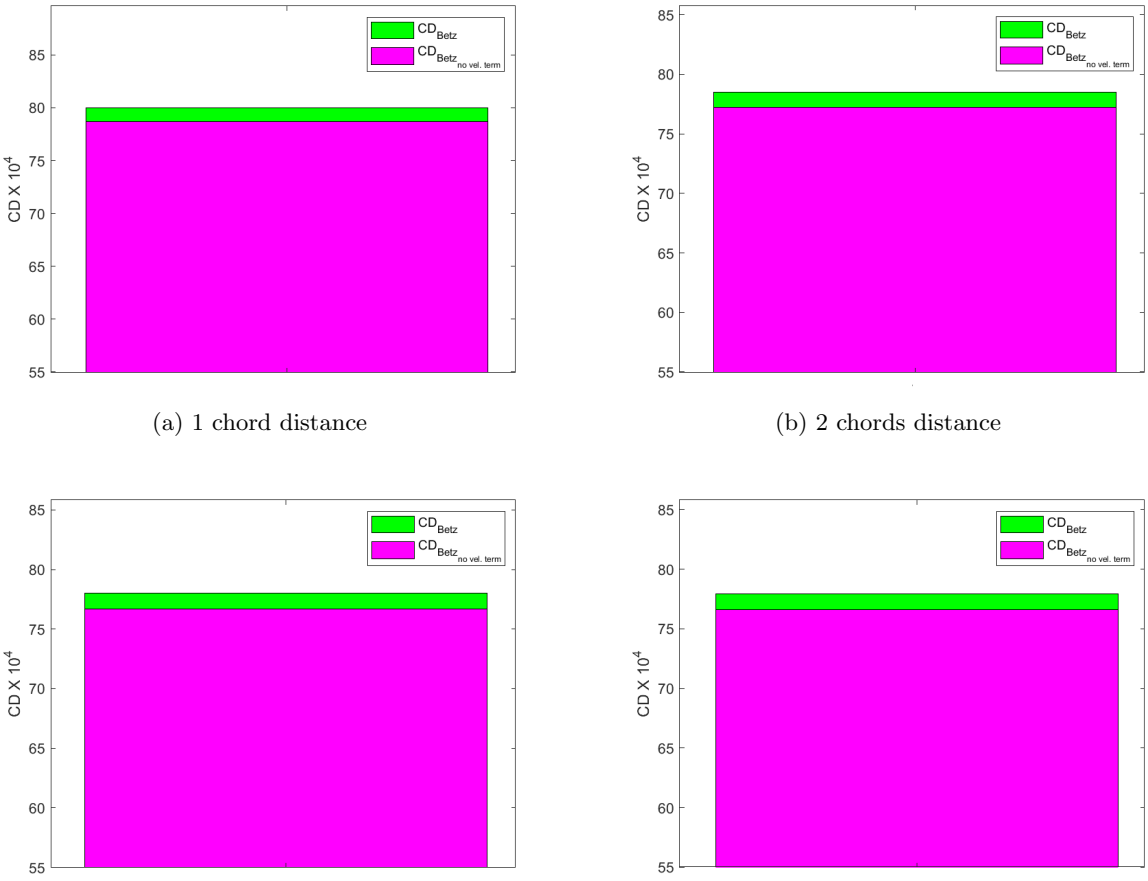

(a) 1 chord distance

(b) 2 chords distance

(c) 3 chords distance

(d) 4 chords distance

Figure 4.5: Comparison for each plane between CD_{Betz} and CD_{Betz} neglecting the second integral in the formulation

Chapter 5

Far-field drag decomposition

In this chapter we will focus the attention on the far-field drag breakdown into viscous, wave and induced contributions, starting from the new formulation (4.7) previously introduced. From now on we will refer to it as *far-field drag formula*, since it will be the one in analysis.

The derivation shown is based on the Ph.D. Thesis written by H. Toubin [8].

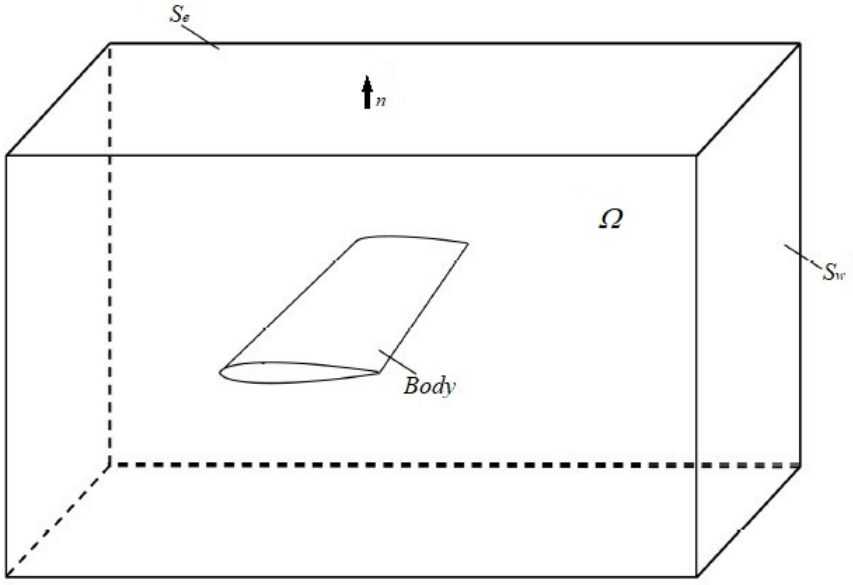

Figure 5.1: Control volume (modified from [8])

5.1 Vector $\boldsymbol{f}$ decomposition

The control volume (fig. 5.1) is the one considered. Upstream the body:

- $u = u_\infty$
- $p = p_\infty$
- $\boldsymbol{\tau_x} = 0$

On the lateral surfaces it is valid to assume that, sufficiently far from the body, the streamlines are aligned to the free stream, so:

- $\boldsymbol{V} \cdot \boldsymbol{n} = 0$
- $\boldsymbol{\tau_x} \cdot \boldsymbol{n} = 0$

We can then write the equation expressing the far-field drag:

$$D_{ff} = \int_{S_w} (\boldsymbol{f} \cdot \boldsymbol{n}) dS \tag{5.1}$$

Considering the wake plane sufficiently far downstream the body and assuming that only irreversible processes in the flow are present, two assumptions can be made:

- $p = p_\infty$
- $v = w = 0$

Under these assumption the irreversible axial velocity on the wake plane S_w is denoted as u_{irr}, whose expression is yet to be derived.

The vector $\boldsymbol{f}$ can be broken down and we obtain the *irreversible* part:

$$\boldsymbol{f_{irr}} = -\rho(u_{irr} - u_\infty)\boldsymbol{V} + \boldsymbol{\tau_x} \tag{5.2}$$

The *reversible* part is the complementary part and can be found by subtracting from $\boldsymbol{f}$ its irreversible part:

$$\boldsymbol{f_{rev}} = \boldsymbol{f} - \boldsymbol{f_{irr}} = -\rho(u - u_{irr})\boldsymbol{V} - (p - p_\infty)\boldsymbol{i} \tag{5.3}$$

From the irreversible and reversible part of the vector $\boldsymbol{f}$ the profile and induced drag can be directly computed as:

$$D_{vw} = \int_{S_w} (\boldsymbol{f_{irr}} \cdot \boldsymbol{n}) dS = \int_{S_w} [-\rho(u_{irr} - u_\infty)\boldsymbol{V} + \boldsymbol{\tau_x}] \cdot \boldsymbol{n} dS \tag{5.4}$$

$$D_i = \int_{S_w} (\boldsymbol{f_{rev}} \cdot \boldsymbol{n}) dS = \int_{S_w} [-\rho(u - u_{irr})\boldsymbol{V} - (p - p_\infty)\boldsymbol{i}] \cdot \boldsymbol{n} dS \tag{5.5}$$

5.2 Irreversible axial velocity

The irreversible axial velocity in the wake plane is defined as u_{irr}. The expression can be derived considering it as a function of the stagnation enthalpy H and the entropy s, so only thermodynamic variables.

Total enthalpy

From the definition of the total enthalpy

$$\Delta H = H - H_\infty = h + \frac{V^2}{2} - \left(h_\infty + \frac{u_\infty^2}{2} \right) \tag{5.6}$$

the velocity can be expressed as

$$V^2 = u_\infty^2 + 2\Delta H - 2(h - h_\infty) \tag{5.7}$$

We then remember that:

$$V^2 = u^2 + v^2 + w^2 \tag{5.8}$$

$$h = C_p T \tag{5.9}$$

Substituting and diving by u_∞^2 we obtain:

$$\frac{u^2}{u_\infty^2} = 1 + \frac{2\Delta H}{u_\infty^2} - \frac{2C_p T_\infty}{u_\infty^2} \left(\frac{T}{T_\infty} - 1 \right) - \frac{v^2 + w^2}{u_\infty^2} \tag{5.10}$$

Entropy

The entropy can be expressed as

$$\Delta s = C_p \ln \left(\frac{T}{T_\infty} \left(\frac{p_\infty}{p} \right)^{\frac{\gamma-1}{\gamma}} \right) \tag{5.11}$$

and rearranging the terms

$$e^{\frac{\Delta s}{C_p}} = \frac{T}{T_\infty} \left(\frac{p_\infty}{p} \right)^{\frac{\gamma-1}{\gamma}} \tag{5.12}$$

5.2.1 Full axial velocity

Using the expressions (5.10) and (5.12) and recalling the definitions of heat capacity (5.13), sound velocity (5.14) and Mach number (5.15)

$$C_p = \frac{R\gamma}{\gamma - 1} \tag{5.13}$$

$$a_\infty = \sqrt{\gamma R T} \tag{5.14}$$

$$M_\infty = \frac{u_\infty}{a_\infty} \tag{5.15}$$

we can write the general expression of the axial velocity:

$$u = u_\infty \sqrt{1 + \frac{2\Delta H}{u_\infty^2} - \frac{2}{(\gamma - 1)M_\infty^2}\left(e^{\frac{\gamma-1}{\gamma}\frac{\Delta s}{R}}\left(\frac{p}{p_\infty}\right) - 1\right) - \frac{v^2 + w^2}{u_\infty^2}} \tag{5.16}$$

We notice that no hypothesis has been made. We have used the definitions of total enthalpy and entropy and than derived the expression for the velocity.

5.2.2 Final expression of u_{irr}

As previously described, the irreversible axial velocity is the velocity present on the wake plane when the assumption of irreversible flow is applied, so that on S_w we have $p = p_\infty$ and $v = w = 0$ (fig. 5.2). By applying these assumptions to (5.16) the final expression of the irreversible axial velocity can be found (5.17). Note that it depends on the variations of entropy and stagnation enthalpy which occur within the shock wave and the boundary layer regions. This means that outside these regions $u_{irr} = u_\infty$.

$$u = u_\infty \sqrt{1 + \frac{2\Delta H}{u_\infty^2} - \frac{2}{(\gamma - 1)M_\infty^2}\left(e^{\frac{\gamma-1}{\gamma}\frac{\Delta s}{R}} - 1\right)} \tag{5.17}$$

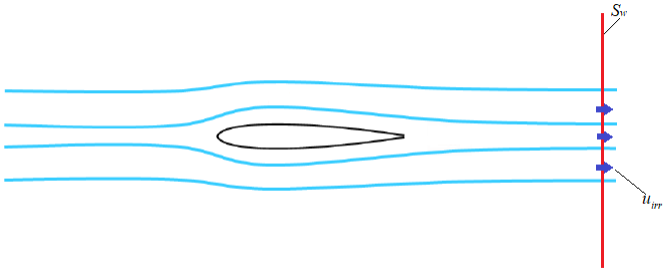

Figure 5.2: Representation of u_{irr} on the wake plane (modified from [8])

5.3 Profile drag decomposition

With the decomposition of the vector $\boldsymbol{f}$ into irreversible and reversible parts the expressions to compute the profile and the induced drag have been found. The profile drag can be further broken down into viscous and wave contributions.

It has been pointed out in chapter 2 that the integrands in Paparone and Tognaccini's formulation (2.8), (2.9) and in Van der Vooren and Destarac's one (2.12), (2.13) for the computation of the viscous and wave drag are the same. This is also the case because we have considered a flow with irreversible processes and this means that thanks to the irreversible part of the vector $\boldsymbol{f}$ the viscous (5.18) and wave drag (5.19) can be computed. The key is to understand the volumes or surfaces which have to be taken into account for the integration.

In order to do so, the use of streamtubes has been considered. The splitting of the surface/volume of integration is artificial since in reality there is an interaction between the boundary layer and the shock. In (fig. 5.3) we can see a schematic splitting. Basically the wake plane is split into a wave part and a viscous part considering where the boundary layer and the wake ends and the region where the shock occurs.

$$D_v = \int_{S_v} (\boldsymbol{f_{irr}} \cdot \boldsymbol{n}) dS \tag{5.18}$$

$$D_w = \int_{S_{sw}} (\boldsymbol{f_{irr}} \cdot \boldsymbol{n}) dS \tag{5.19}$$

In the simulations, since the variations of entropy and total enthalpy in the shock region appear only where the shock itself is present, the shock plane of integration can be moved closer to the wave drag source to avoid numerical diffusion or grid effects.

The integration in the viscous region has to take into account the enlargement of the wake when moving downstream.

We will see in the following simulations how these aspects have been considered and how the planes of integrations have been chosen.

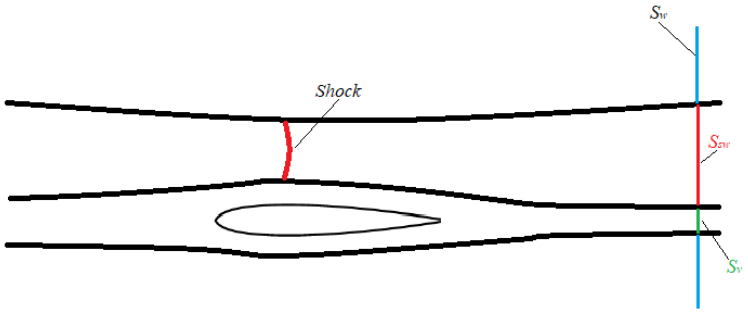

Figure 5.3: Schematic representation of streamtubes and surface splitting

Chapter 6

Far-field drag decomposition, 2D steady simulations

In this chapter four different 2D simulations will be analyzed and the far-field drag decomposition will be implemented. In the integration the term $\boldsymbol{\tau_x}$ is neglected as explained in chapter 4.

Since the conducted simulation are two-dimensional, the induce drag is therefore absent.

For each simulation, as shown in chapter 4, the general aspects, the model used and the grid are presented. Afterwards, it will be conducted the analysis on how the *far-field drag formula* and the drag decomposition have been implemented and how the surfaces of integration have been constructed.

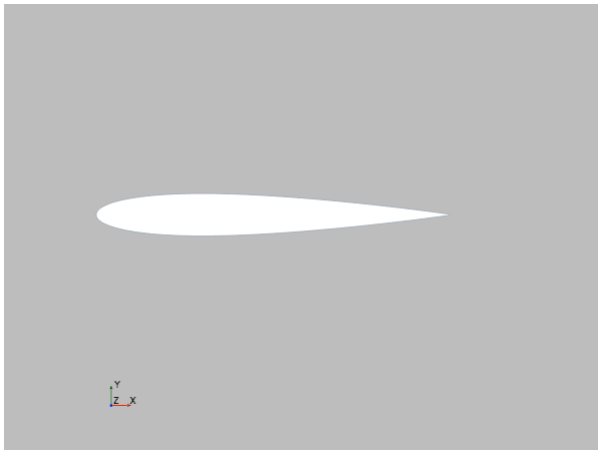

Figure 6.1: NACA0012 airfoil

All the simulations are conducted at $Re = 3 \cdot 10^6$ and are performed on the NACA0012 airfoil (fig. 6.1) at angle of attack $\alpha = 0°$ with chord $c = 1[m]$. The domains extend for 200 chords both upstream and downstream the airfoil.

6.1 Simulation $Mach = 0.2$

The aim of this simulation is to show that, since the Mach number is $M = 0.2$ and as a consequence the compressibility effects can be neglected, theoretically from the drag decomposition we should be able to verify that the only drag contribution comes from the viscous drag.

6.1.1 Simulation setup

Here are reported the characteristics of the model:

- two dimensional
- solution interpolation
- steady
- ideal gas
- coupled flow, coupled energy
- RANS (Reynolds-Averaged Navier-Stokes) equations
- turbulent with K-Omega turbulence (SST Menter)
- wall distance, all $y+$ wall treatment

The ratio of specific heats is $\gamma = 1.4$ and the specific gas constant is $R = 287.05[J/(kgK)]$. From the Reynolds definition (3.1) the density can be calculated, $\rho_\infty = 0.7413[kg/m^3]$. The reference static pressure is computed from (1.11), $p_\infty = 63,838.6843[Pa]$ and the initial conditions are static pressure $p = 0[Pa]$, static temperature $T = 300[K]$ and velocity found from (3.3), $u_\infty = 69.4438[m/s]$

The boundary conditions are:

- *wall* type for the airfoil
- *stagnation inlet*, with total pressure and temperature computed from the isentropic formulas
- *pressure outlet*

The mesh is realized using a polygonal mesher, with he final grid presenting a total of 716,073 cells. In fact the refinement in the wake has been realized quite fine in order to avoid diffusion.

The wake will not be so fine in the following simulations, but here the aim is to analyze only the contribution in the wake, so it is fair to be more strict for this analysis.

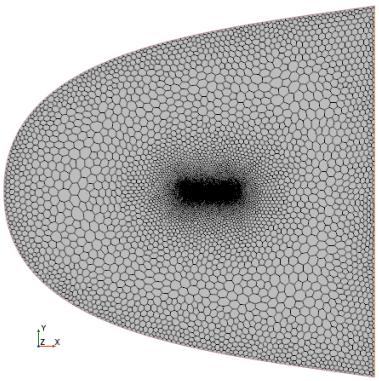

(a) Domain

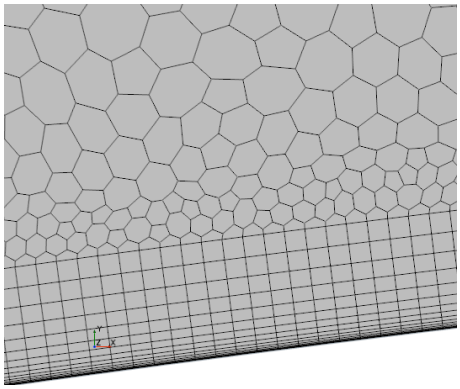

(b) Prism layer zoom

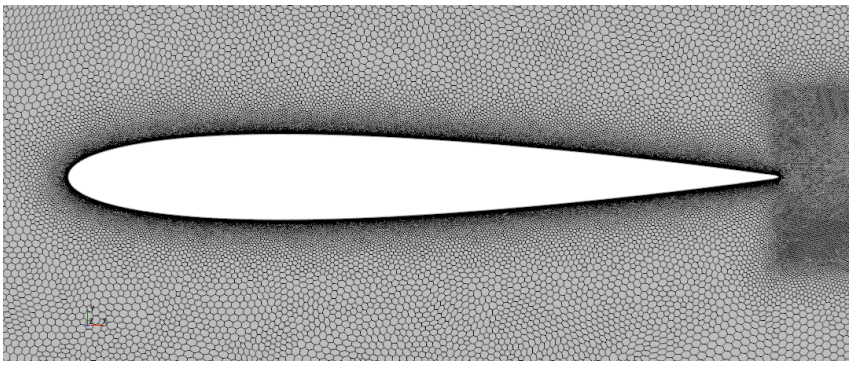

(c) Airfoil zoom

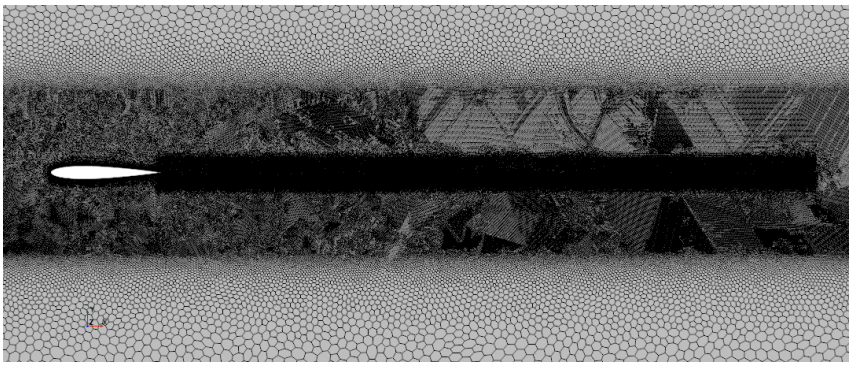

(d) Wake refinement

Figure 6.2: Grid scenes

6.1.2 Post-processing and results

The simulation reaches convergence in about 4,800 iterations.

The irreversible axial velocity u_{irr} is computed from (5.17). We have observed that for consistency of the simulation, the values of total enthaply and entropy at infinity for the computation of ΔH and Δs are better to be found with an evaluation really far from the airfoil (close to the end of the domain) with a *line probe* rather than using the formulas. This is probably better because it takes into account the evolution of the simulation including spurious effects.

Differently from what has been done in chapter (4),the command *constrained plane*, with the planes defined using *macro* in order to realize a plane with precise coordinates, has not been used. Instead the integration has been done by applying a constriction directly to the formula (we refer to (A.1)) and perform a surface integral considering a *plane section*. This problem is shown more accurately in Appendix A.

To chose the y coordinate in order to write the expressions of the formulas, here is reported the wake of the simulation (fig. 6.3a), useful for the extraction of the viscous drag.

The wake can be visualized for example from the velocity, total enthalpy or entropy scenes, by making a right choice of the scalar field of the scene itself. For each distance we select the coordinate and write it in the implementation of the field function $\boldsymbol{f_{irr}}$. It is clear that since the wake grows moving downstream, for each distance the coordinate has to be changed, in order to follow the wake growth itself (fig. 6.3b). By making this work, the results obtained are consistent.

We perform the surfaces integral, applying (5.18) and (5.1), comparing both results with the near-field drag (fig. 6.5).

The value of the near-field drag coefficients is $CD_{nf} = 88.7352$ drag counts. The far-field drag coefficient confirms the accuracy with a convergence value of around $CD_{ff} \simeq 89.1$ drag counts, producing an error of 0.41% with the near-field one. The viscous drag coefficient reaches a convergence at around the value of $CD_v \simeq 86.85$ drag counts, with an error of 2.12%.

We note that initially the value of viscous drag is quite close to the near-field, but then decreases a bit. Probably thanks to the fine prism layer the boundary layer and the first part of the wake are well captured, then we encounter some spurious effects.

(a) Wake

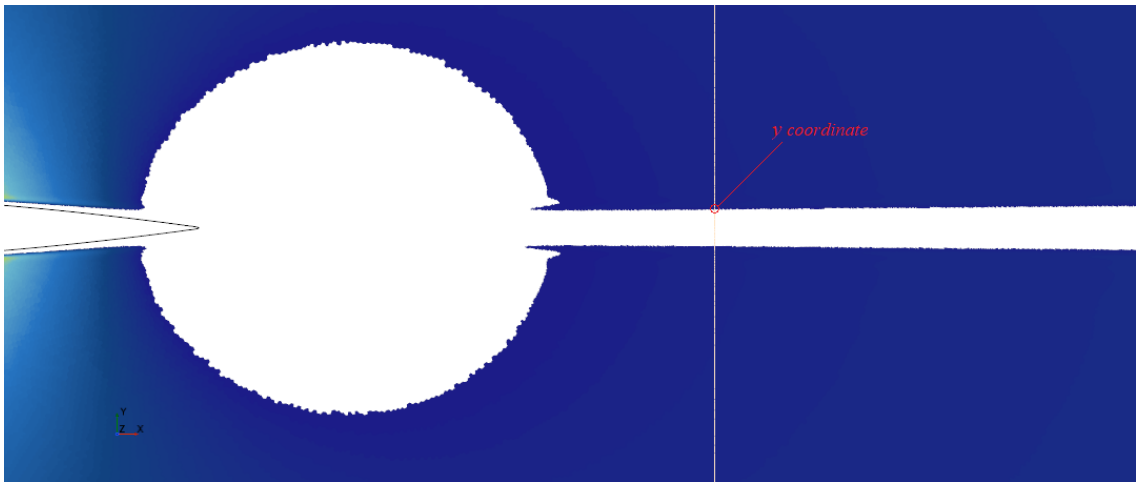

(b) Choice of the y coordinate on the *plane section*

Figure 6.3: Wake scenes

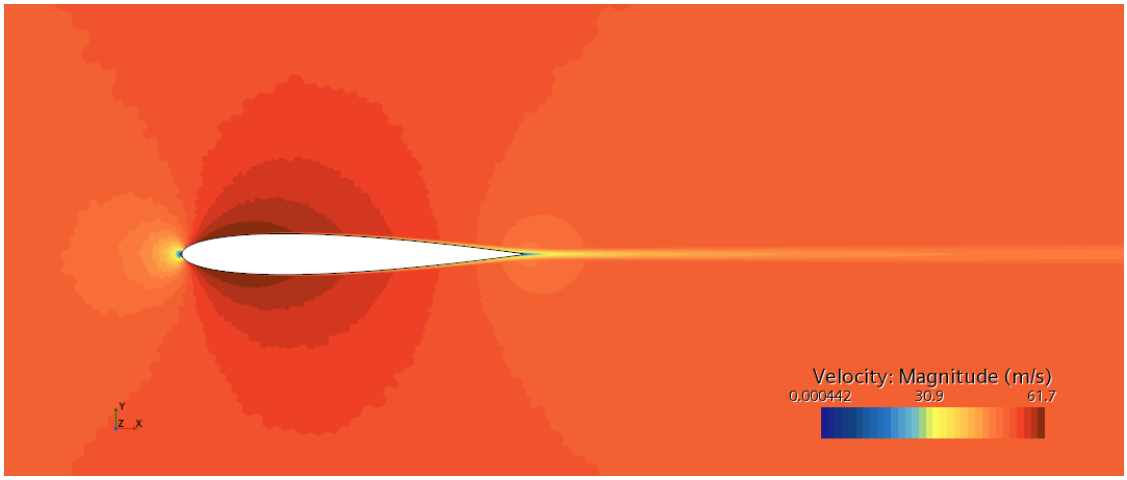

Figure 6.4: Velocity scene

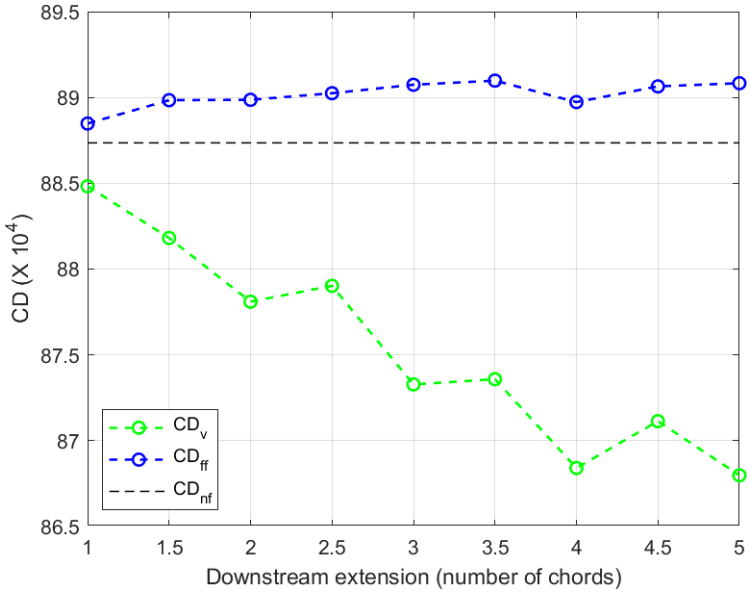

Figure 6.5: Final results. CD_v , CD_{ff} , CD_{nf} expressed in drag counts

6.2 Simulation $Mach = 0.8$, inviscid case

The aim of this simulation is basically the same of the previous one but regarding the wave drag extraction. Since the simulation involves a non-viscous flow, the total drag is theoretically the wave drag and this is what we try to verify here.

6.2.1 Simulation setup

The characteristics of the model used are the following:

- two dimensional
- solution interpolation
- steady
- ideal gas
- coupled flow, coupled energy
- inviscid
- Euler equations

The ratio of specific heats is $\gamma = 1.4$ and the specific gas constant is $R = 287.05[J/(kgK)]$. From the Reynolds definition (3.1) the density can be calculated, $\rho_\infty = 0.1932[kg/m^3]$. The reference static pressure is computed from (1.11), $p_\infty = 16,642.3283[Pa]$ and the initial conditions are static pressure $p = 0[Pa]$, static temperature $T = 300[K]$ and velocity found from (3.3), $u_\infty = 277.7752[m/s]$

The boundary conditions are:

- *wall* type for the airfoil
- *stagnation inlet*, with total pressure and temperature computed from the isentropic formulas
- *pressure outlet*

The mesh is realized using a polygonal mesher, and the final grid presents a total of 162,328 cells.

A shock refinement is performed, using a field function defined in *STAR-CCM+* as

$$log(mag(grad(\$MachNumber))) \tag{6.1}$$

and defining through position commands the region of the domain where to be applied.

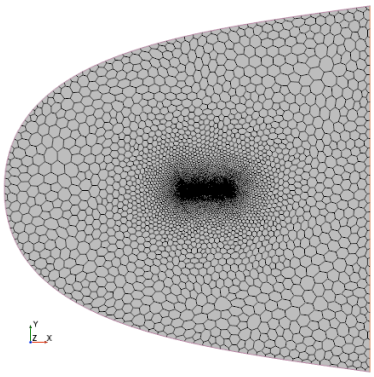

(a) Domain

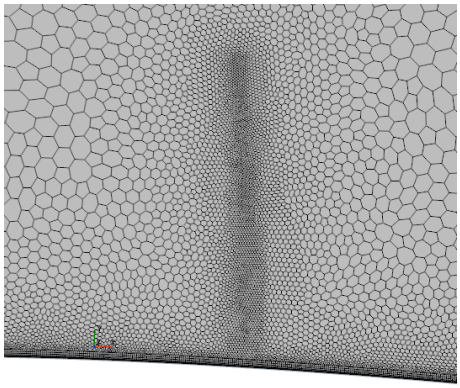

(b) Shock refinement zoom

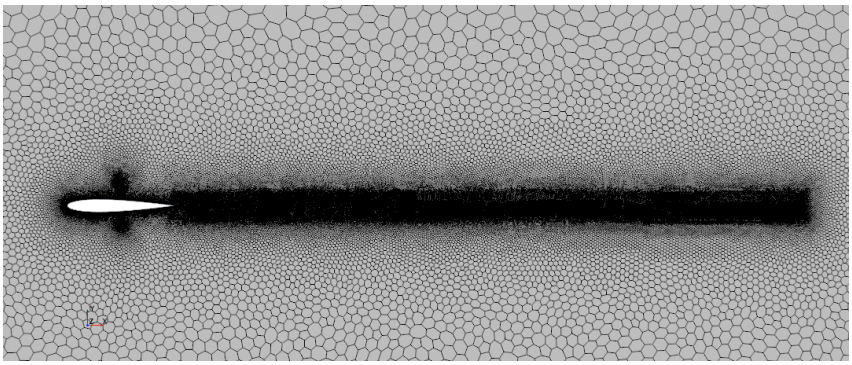

(c) Wake zoom

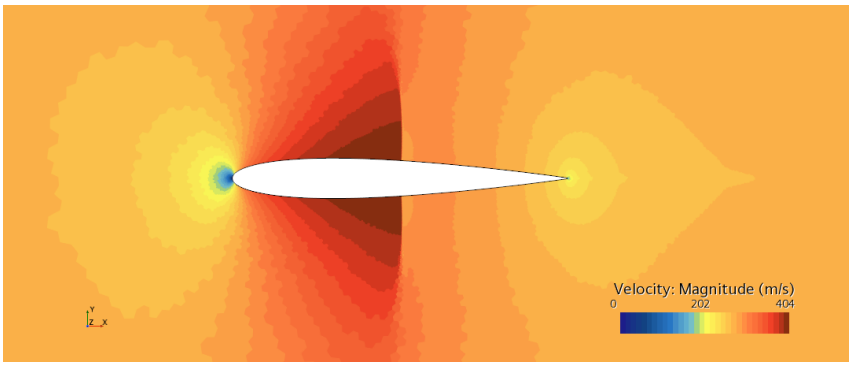

(d) Velocity scene

Figure 6.6: Simulation scenes

6.2.2 Post-processing and results

This simulation reached convergence in about 10,600 iterations which may look quite a lot. The problem encountered was that the shocks, above and below the airfoil, were moving forward and backward alternatively and the simulation struggled to reach convergence despite the refinements in the wake and shock regions.

This problem was not present in the simulations at $M = 0.8$ which will be presented later in the chapter, so we assumed that the problem comes from the inviscid simulation itself.

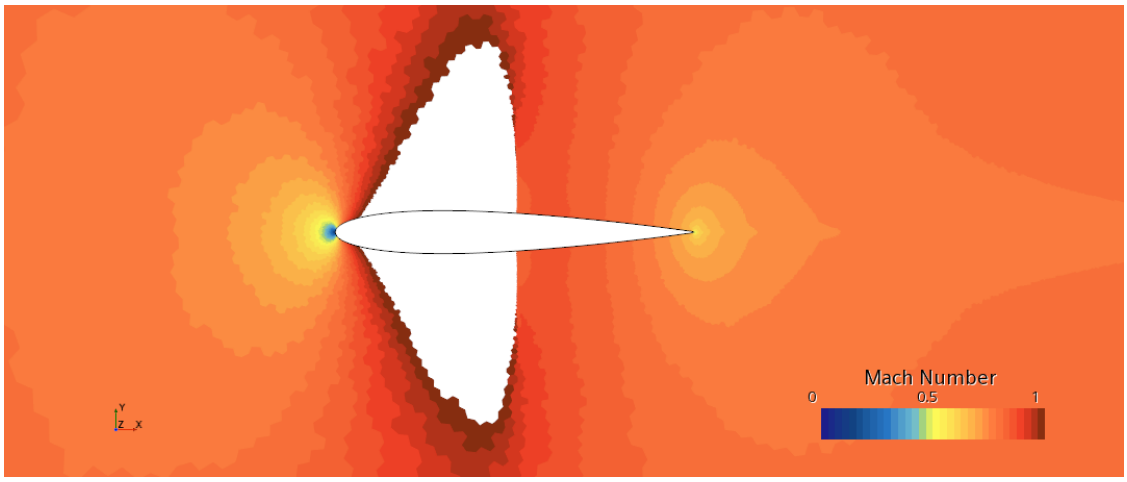

Figure 6.7: Mach scene

The post-processing is the same previously described, u_{irr} is computed from (5.17), the integrations are performed on plane sections modifying the field functions written for $\boldsymbol{f_{irr}}$.

If we look at (fig. 5.3), we observe that since no boundary layer is present here, the integration is performed on a length of plane S_{sw} that goes from point to point in height as visible in (fig. 6.7).

We compute the near-field drag, the far-field drag from (5.1) and the wave drag from (5.19). The near-field drag coefficient has a value of $CD_{nf} = 85.4272$ drag counts. The far-field coefficient is about $CD_{ff} \simeq 86.7$ drag counts and the wave one is about $CD_w \simeq 82.1$ drag counts. The far-field drag coefficient produces a difference with the near-field one of 1.48% and the wave drag coefficients 3.89%, which is quite a big margin even if compared to the previous case of the viscous drag.

From the results obtained (fig. 6.8) it is clearly visible that the values have a good convergence but probably there are some spurious effects which derives from the difficulty of performing the simulation described before.

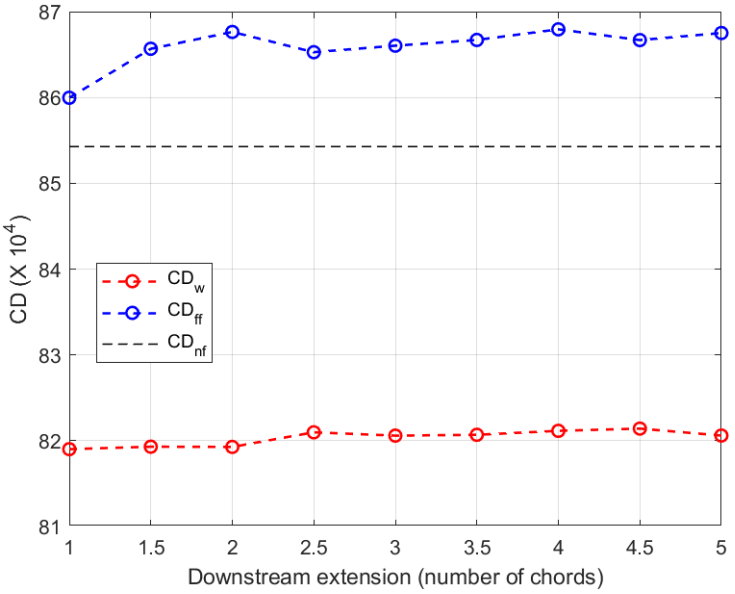

Figure 6.8: Final results. CD_v , CD_{ff} , CD_{nf} expressed in drag counts

6.3 Simulation $Mach = 0.8$

We have analyzed cases where theoretically only one between viscous or wave drag was present.

Now we focus the attention on a case in which both appear, trying to extract the profile drag decomposed in the two contributions of viscous and wave drag. It is basically the case previously described but the difference is that the flow is not inviscid anymore, so boundary layer and wake are present and as a consequence the viscous drag component.

6.3.1 Simulation setup

Here are reported the characteristics of the model:

- two dimensional
- solution interpolation
- steady
- ideal gas
- coupled flow, coupled energy
- RANS (Reynolds-Averaged Navier-Stokes) equations
- turbulent with K-Omega turbulence (SST Menter)
- wall distance, all $y+$ wall treatment

The ratio of specific heats is $\gamma = 1.4$ and the specific gas constant is $R = 287.05[J/(kgK)]$. From the Reynolds definition (3.1) the density can be calculated, $\rho_\infty = 0.1853[kg/m^3]$. The reference static pressure is computed from (1.11), $p_\infty = 15,959.6711[Pa]$ and the initial conditions are static pressure $p = 0[Pa]$, static temperature $T = 300[K]$ and velocity found from (3.3), $u_\infty = 277.7752[m/s]$

The boundary conditions are:

- *wall* type for the airfoil
- *stagnation inlet*, with total pressure and temperature computed from the isentropic formulas
- *pressure outlet*

The mesh is realized using a polygonal mesher, and the final grid presents a total of 229,556 cells. In this case a shock refinement has not been performed, as visible in (fig. 6.9c).

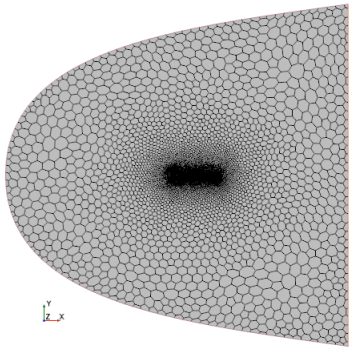

(a) Domain

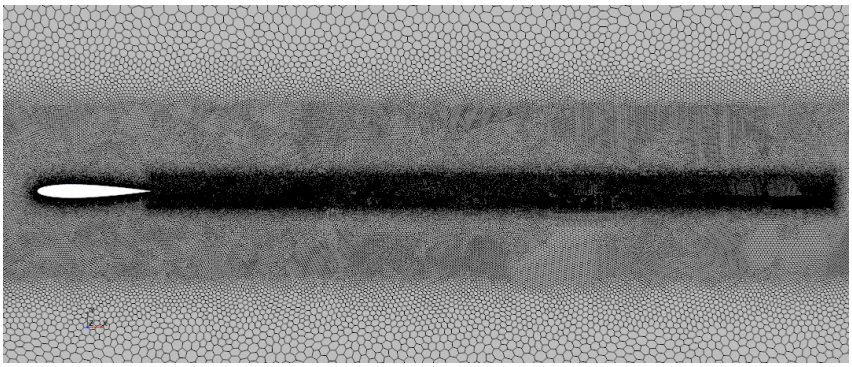

(b) Wake zoom

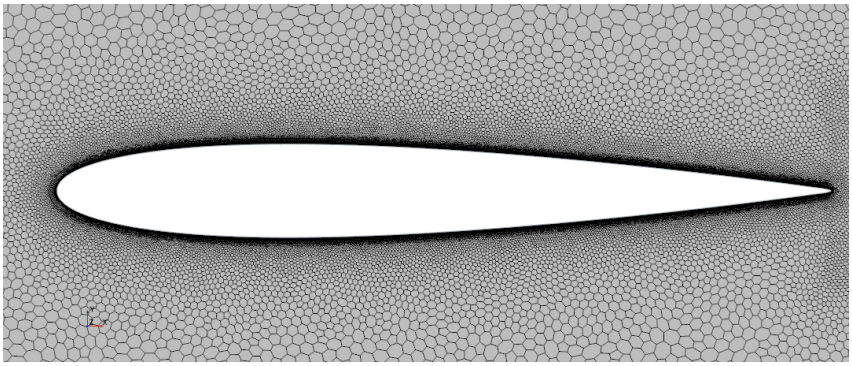

(c) Airfoil zoom

Figure 6.9: Grid scenes

6.3.2 Post-processing and results

The convergence of the simulation is reached after about 4,300 iterations.

As always we compute u_{irr} from (5.17) and with the expressions (5.1), (5.18) and (5.19) we are able to extract respectively the far-field, the viscous and the wave drag.

From the entropy scene (fig. 6.10a), as described in section 6.1, we are able to find the coordinates to perform the correct integration of the viscous drag.

To perform the wave drag integration we move close to the shock, carefully choosing the coordinate in order not to interfere with the boundary layer (fig. 6.10c). As already explained in the document, it is clear that this is an artificial splitting since in reality the shock and the boundary layer interact together.

In (fig. 6.11) the results of the simulation are presented. The viscous drag coefficient CD_v seems to reach convergence at around 120 drag counts but the last point is around 122 drag counts. The wave drag coefficient settles at around $CD_w \simeq 52$ drag counts. The near-field drag coefficient is $CD_{nf} = 169.8065$ and the resulting far-field one is $CD_{ff} \simeq 171.5$ with a difference of 0.99%. The sum $(CD_v + CD_w)$, i. e. the profile drag, which is theoretically the total drag, is about 172 to 174 drag counts.

In this case the values of the drag decomposition seems to be more accurate than the previous cases.

(a) Entropy scene

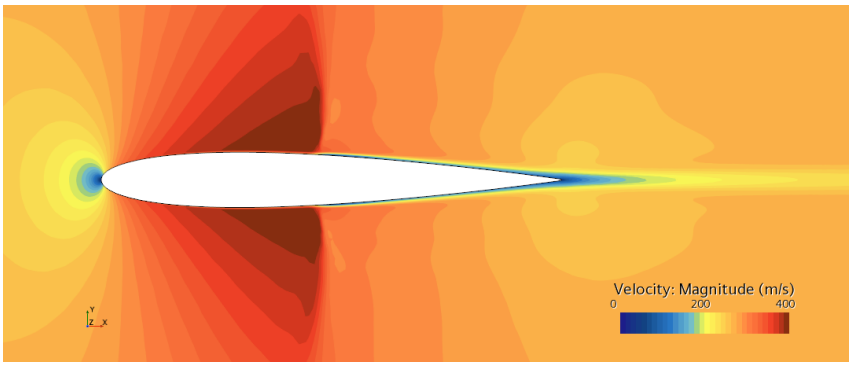

(b) Velocity scene

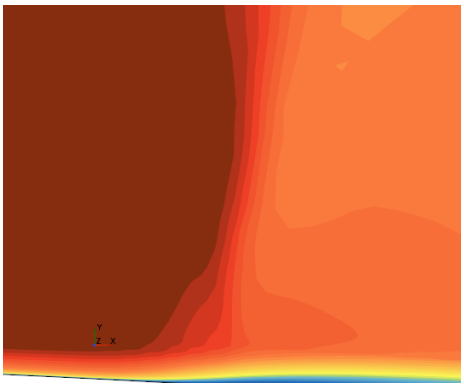

(c) Shock and boundary layer zoom

Figure 6.10: Simulation scenes

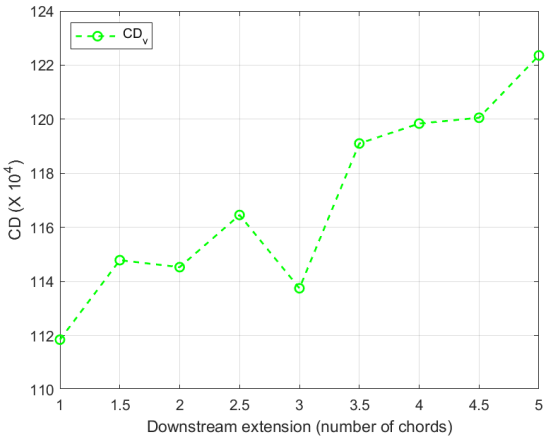

(a) CD_v (drag counts)

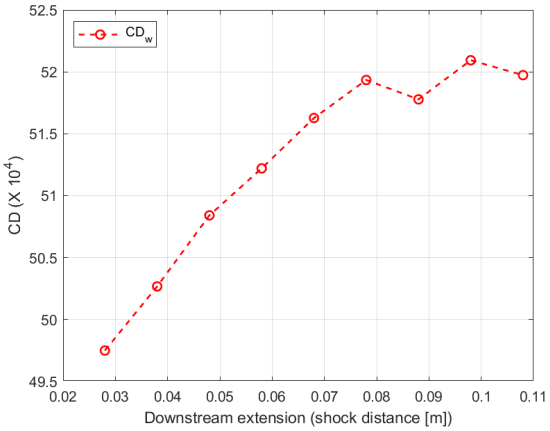

(b) CD_w (drag counts)

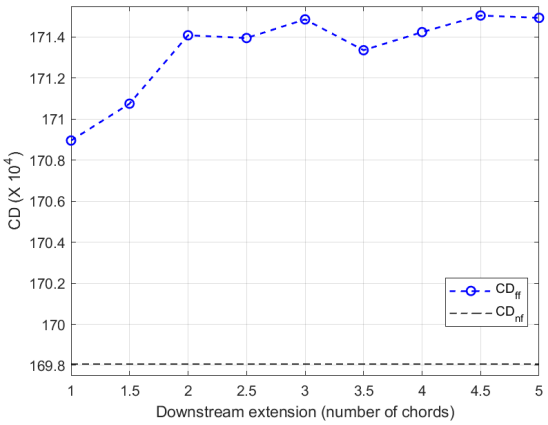

(c) CD_{ff}, CD_{nf} (drag counts)

Figure 6.11: Final results

6.4 Simulation $Mach = 0.8$ with adaptive mesh refinement

This simulation is the same case of the previous one (section 6.3) but with adaptive mesh refinement applied (AMR). We would like to analyze the changes in the results of the resulting drag contributions when AMR is performed.

6.4.1 Simulation setup

The characteristics of the model and the boundary conditions are the same presented in section (6.3).

The grid is realized defining a *shock sensor* in the *field function* section, using again the expression

$$log(mag(grad(\$MachNumber))) \tag{6.2}$$

and the total enthaply. Combining these information to create a sensor, it is possible to realize a mesh refinement in the shock region (fig. 6.12b). The final grid has a total of 252,097 cells.

6.4.2 Post-processing and results

The simulation reaches convergence after about 5,000 iteration,

All the steps to extract the results are the same described in the previous section (6.3) and in (fig. 6.13) we can see the results. The viscous drag coefficient CD_v reaches a value of around 117.5 drag counts but the values seems a bit more variable than before. The wave drag coefficient, thanks to the shock refinement, has a very little variability with a convergence at around $CD_w \simeq 50.35$ drag counts. The near-field drag coefficient is $CD_{nf} = 169.6947$ (slightly different than before) and the resulting far-field one is $CD_{ff} \simeq 171.5$ with a difference of 1.06%. The sum $(CD_v + CD_w)$, is around 168 drag counts.

The evaluation of the viscous drag may look less accurate than the previous simulation. Probably this is due to the fact that using an adaptive refinement for the shock creates a faster transition from smaller to bigger cells and this could induce some sort of numerical diffusion, even because from the results it is clear that the shock is better capture. Using an AMR for the shock region could mean that even a greater refinement in the wake should be made.

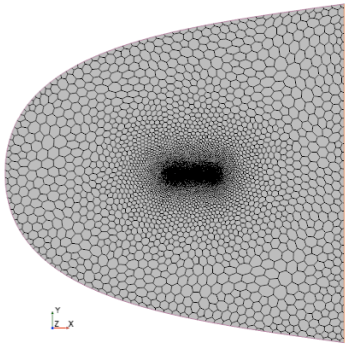

(a) Domain

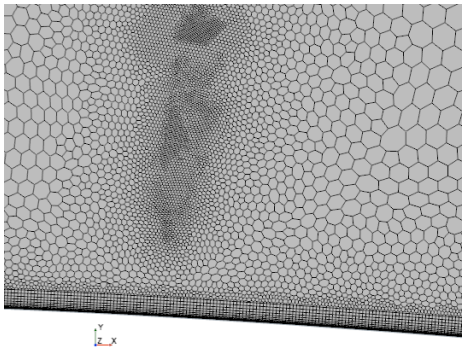

(b) Shock refinement zoom

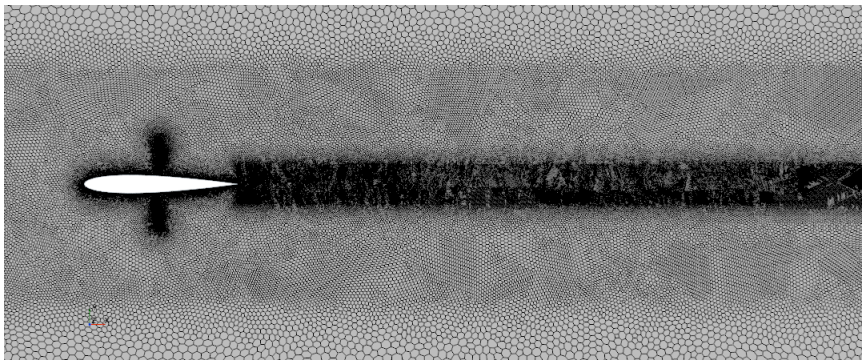

(c) Airfoil, shock and wake zoom

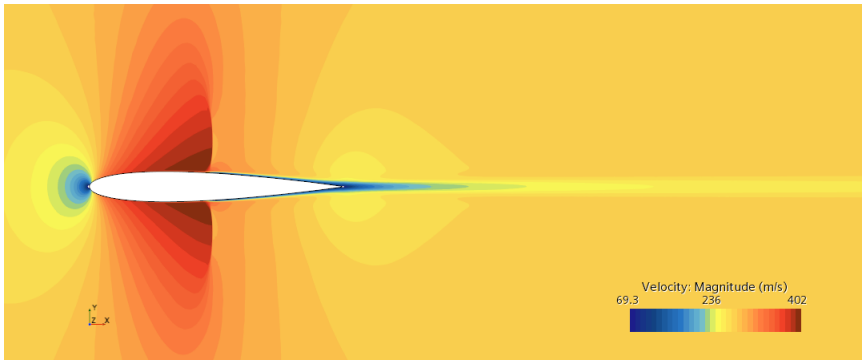

(d) Velocity magnitude scene

Figure 6.12: Simulation scenes

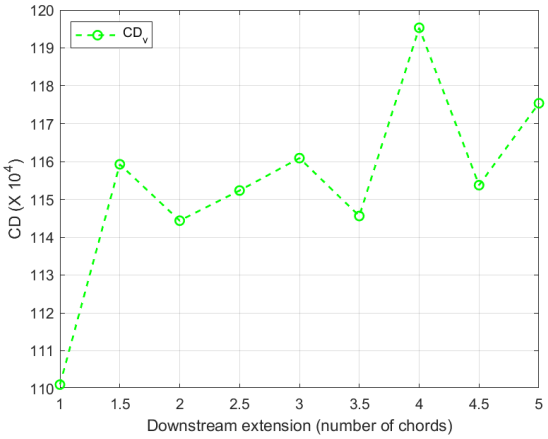

(a) CD_v (drag counts)

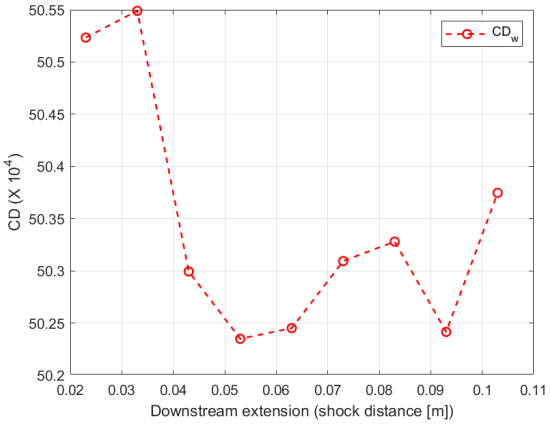

(b) CD_w (drag counts)

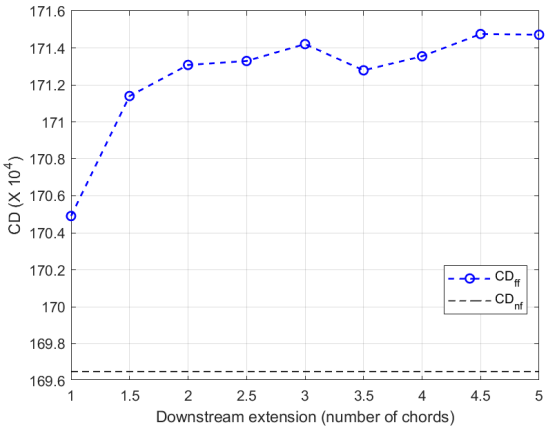

(c) CD_{ff}, CD_{nf} (drag counts)

Figure 6.13: Final results

Chapter 7

Far-field drag decomposition, 3D steady simulation

In the previous chapter a series of two-dimensional simulations have been studied to perform a far-field drag decomposition. In this one a 3D simulation is presented as a direct comparison with the one presented by H. Toubin in the work of Thesis ([8], pp. 81 to 84).

Clearly this is a closer case to reality even if the wing is extremely simple but this allows to extract the induced drag component from the drag breakdown into its contributions, which was previously absent.

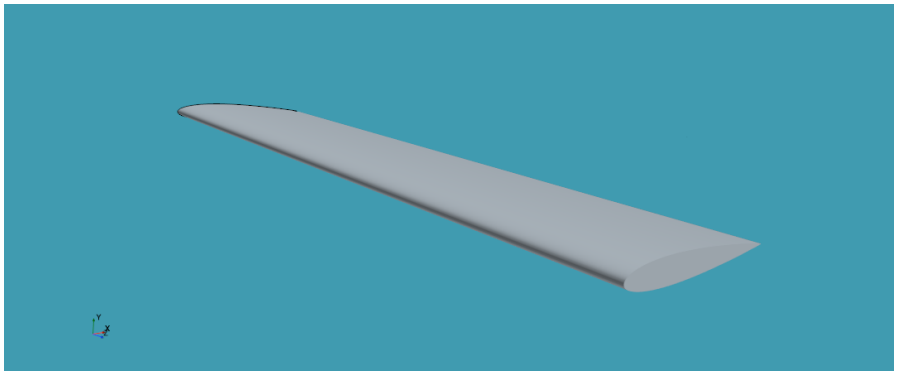

Figure 7.1: Rectangular wing of the simulation

7.1 3D simulation

The simulation is performed on a rectangular wing with aspect ratio of 8 (fig. 7.1). The airfoil of the wing is the NACA0012, with constant chord $c = 1[m]$ along the wing span. The Mach number is $M = 0.8$, the Reynolds number is $Re = 2.7 \cdot 10^6$ and the angle of attack is $\alpha = 2.5°$.

7.1.1 Setup

The model presents the following characteristics:

- three dimensional
- solution interpolation
- steady
- ideal gas
- coupled flow, coupled energy
- RANS (Reynolds-Averaged Navier-Stokes) equations
- turbulent with K-Omega turbulence (SST Menter)
- wall distance, all $y+$ wall treatment

The ratio of specific heats is $\gamma = 1.4$ and the specific gas constant is $R = 287.05[J/(kgK)]$. From the Reynolds definition (3.1) the density can be calculated, $\rho_\infty = 0.1803[kg/m^3]$. The reference static pressure is computed from (1.11), $p_\infty = 15,527.8671[Pa]$ and the initial conditions are static pressure $p = 0[Pa]$, static temperature $T = 300[K]$ and velocity found from (3.3), $u_\infty = 277.7752[m/s]$

The boundary conditions are:

- *wall* type for the airfoil
- *simmetry plane* for the domain
- *stagnation inlet*, with total pressure and temperature computed from the isentropic formulas
- *pressure outlet*

The mesh is realized using a trimmed cell mesher, and the final grid presents a total of 20,392,302 cells with an extension of 200 chords both upstream and downstream the wing. As visible in (fig. 7.2b) and (fig. 7.2c) a mesh refinement has been performed in order to better capture the shock and the wake. The refinement in the wake is realized with the use of blocks, changing the size type relative to the base one through custom controls. A series of field functions has been written but they are all based on the expression already shown in the previous chapter

$$log(mag(grad(\$MachNumber))) \tag{7.1}$$

and taking in consideration the wall distance and the total enthaply it is possible to define a *shock sensor* thanks to which a refinement in the shock region itself can be performed.

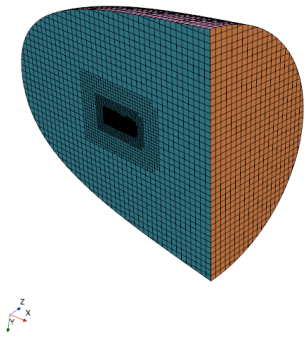

(a) Domain

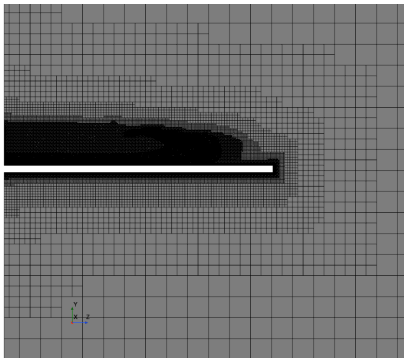

(b) Grid refinement

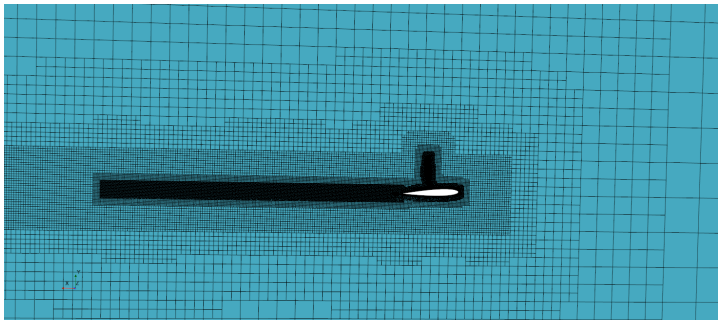

(c) Wake and shock refinement zoom

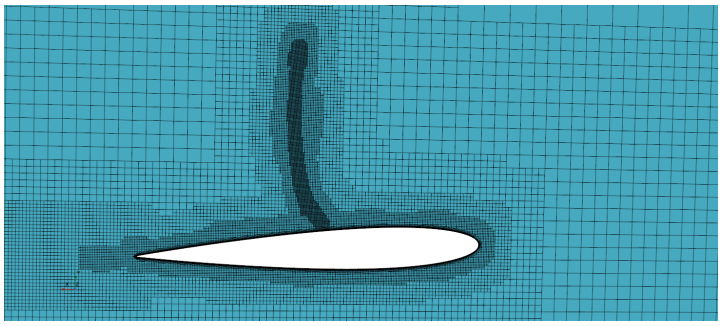

(d) Airfoil zoom

Figure 7.2: Mesh scenes

7.1.2 Post-processing and results

The simulation well converges after about 5,000 iterations.

As always we compute u_{irr}, $\boldsymbol{f}$, $\boldsymbol{f_{irr}}$ and in this case $\boldsymbol{f_{rev}}$. Thanks to the equation (5.1), (5.18), (5.19), (5.5) we can evaluate respectively the far-field drag, the viscous drag, the wave drag and the induced drag.

The surface of integration for the computation of the far-field drag and the induced one is the same and it is realized with a *constrained plane*, far from the airfoil 3 chords length (we extend at the limit of 3 chords because after that distance the mesh becomes more coarse).

Differently from what has been done in chapter (6), the integration for the viscous and wave drag as not been done using the equation (A.1). The constriction on $\boldsymbol{f_{irr}}$ has been done considering the vorticity and creating a field function for the viscous drag. In order to perform its computation, a plane section is considered downstream the wing. On this plane we consider the vorticity (fig. 7.4a), (fig. 7.4b) and we can write an expression of $\boldsymbol{f_{irr}}$ for the viscous drag defined as '*f irr viscous sensor*' (Appendix B). In this way the integration is performed on a plane section but only in the zone where $\boldsymbol{f_{irr}}$ is defined (fig. 7.4c). A similar argument is done for the wave drag, creating a '*f irr shock sensor*', using the information already used to realize the refinement.

For the computation of the viscous drag a plane section at 3 chords distance is considered whereas for the wave drag a plane section at a distance of $0.027155[m]$ from the shock.

In table (7.1) we can see the comparison of the results obtained from H. Toubin and this simulation, where the drag coefficients are expressed in drag counts. The values of the near-field drag coefficents are slightly different but the domains and the boundary conditions are different. The value of the far-field drag coefficient obtained in this simulation confirms the accuracy of the formulation with a difference of 0.66% from the near-field one. The induced drag coefficients are about the same for both simulations. A discrepancy can be seen from the viscous and wave drag coefficients, but this can depend from various factor, such as the choice of the regions where the shock and the wake are split or the fact that in this simulation we have performed surface integrals whereas H. Toubin has performed volume integrals. However it is interesting to notice that the sum $(CD_v + CD_w)$, i. e. the profile drag, is about the same (1 drag count of difference).

	H. Toubin simulation	**Current simulation**
CD_{nf}	283.31	279.01
CD_{ff}	–	280.85
CD_v	$\simeq 154$	$\simeq 165$
CD_w	$\simeq 104$	$\simeq 92$
CD_i	$\simeq 27$	$\simeq 27$

Table 7.1: Simulations results

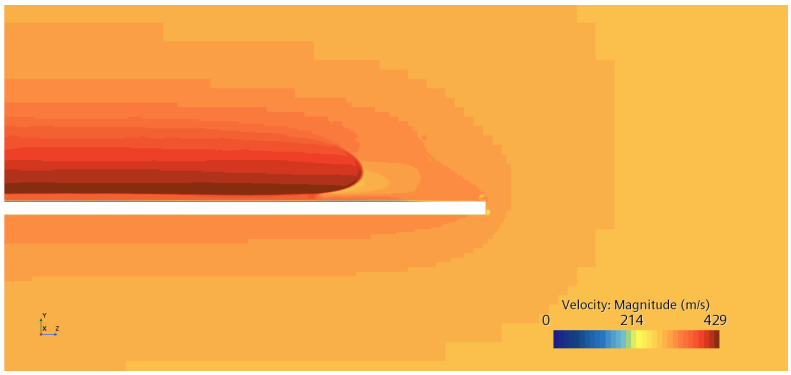

(a) Velocity scene

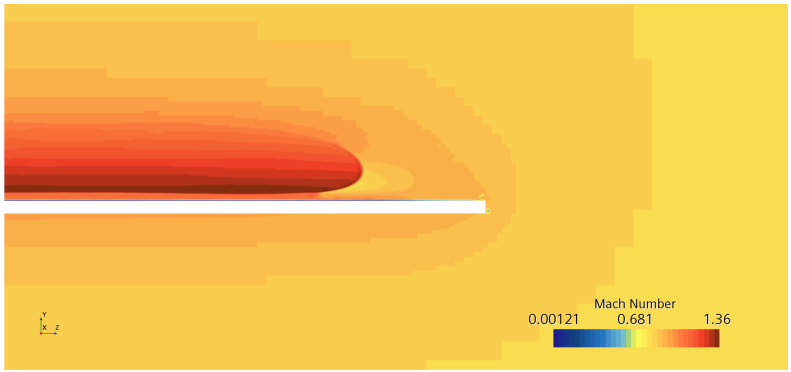

(b) Mach scene

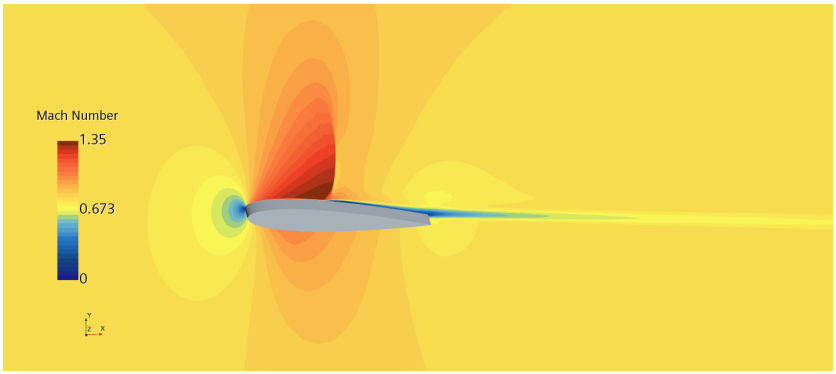

(c) Mach scene (different angle)

Figure 7.3: Simulation scenes

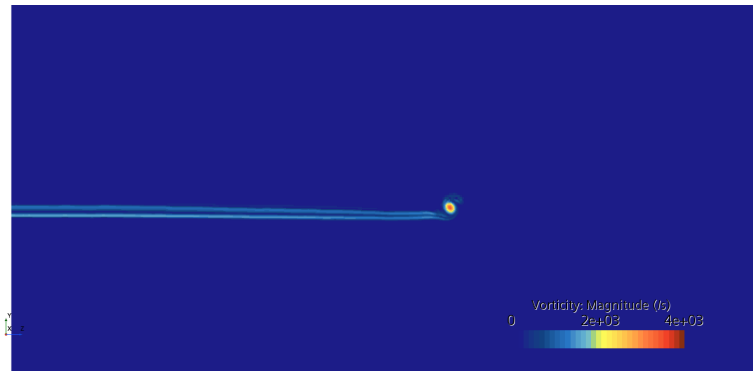

(a) Vorticity scene

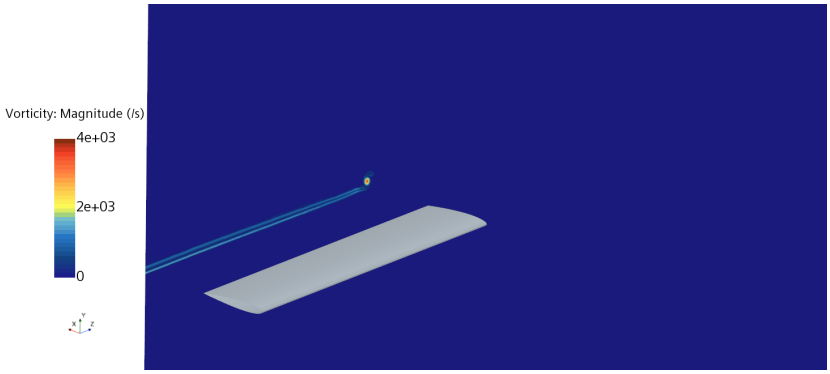

(b) Vorticity scene (different angle)

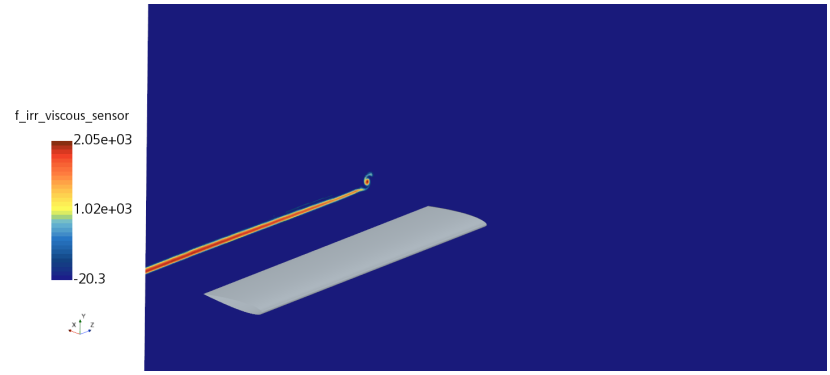

(c) '*f irr viscous sensor*' area of integration

Figure 7.4: Visualization of the zone of integration for $\boldsymbol{f_{irr}}$

Chapter 8

Conclusions

From the simulations conducted in this document it is fair to say that the far-field methods are a great tool for the analysis of the aerodynamic performances.

The application in a commercial CFD software has produced a satisfactory accuracy in the results, but here only preliminary studies have been done.

We have analyzed simple cases and for each case we have extracted the various contributions of drag. The convergence of the viscous drag values has proven to be critical, depending on the grid realization and the refinement performed in the wake region, whereas the values of the wave drag seems to be more precise to capture. The values obtained for the total drag with the far-field drag formula and for the induced drag are very satisfactory.

It is clear that the power of this methods implies various issues. The key point is the difference in the integration with the near-field where this is performed on the surface of the body, so the physical object of interest is defined. The construction of the various plane or volumes and where to distinguish the various region is the main problem, moreover if a substantial more complex flow is analyzed, such as the wake produced by an entire aircraft, it is clear that different criteria should be taken into account for the correct integration, as an example the one which has been presented in chapter 7.

I personally think that if this tool is well supported, in a world where details matters more and more, the application of these methods can lead to new concepts in aircraft design and aerodynamic performances.

Appendix A

Far-field drag decomposition, 2D steady simulations

A.1 Integration note

In chapter 6 has been explained that for the integration, differently from what has been done in the simulation in chapter 4, the command *constrained plane* has not been used, but the integrations have been made considering a *plane section* and implementing the formulas for the computation of total, viscous and wave drag with a constriction in the zone where to perform the integrations.

This has been done because a problem of inconsistency has been noticed when using constrained planes. After completing a number of iterations, the post-processing is made and the results extracted. When making more iterations, suddenly the values obtained from the planes integration change (fig. A.1). Actually the cause has not been found.

As previously said, the problem has been avoided with the constriction not on the plane but on the formula itself, implemented as

$$\{\boldsymbol{f_{irr}} = -\rho(u_{irr} - u_\infty)\boldsymbol{V} + \boldsymbol{\tau_x}\} * (|y| < \mathit{coordinate}) \tag{A.1}$$

with the expression

$$|y| < \mathit{coordinate} \tag{A.2}$$

equals to 1 only in the regions of interest.

By performing an integration on a *plane section* of the formula implemented as shown above, we observed that the values were consistent again and the post-processing could be made correctly.

Figure A.1: Values discrepancy when performing new iterations

Appendix B

Far-field drag decomposition, 3D steady simulation

B.1 Viscous sensor field functions

Here are reported the field functions written in *STAR-CCM+* to perform the shock refinement and the integration for the extraction of the viscous drag, as explained in chapter 7.

$$\$ShockSensor = (\$TotalEnthalpy > 3.396e+05)\&\& \\ ((log(mag(grad(\$MachNumber)) * pow(\$Volume, 1/3))) > -2)?1 : 0 \quad \text{(B.1)}$$

$$\$AMR\_Shock = \$ShockSensor > 0.99?0.005 : 0 \quad \text{(B.2)}$$

$$\$Viscoussensor1 = mag(\$\$VorticityVector) > 200?1 : 0 \quad \text{(B.3)}$$

$$\$Viscoussensor2 = div(grad(\$MachNumber)) > 20?1 : 0 \quad \text{(B.4)}$$

$$\$viscoussensor = (\$Viscoussensor1 + \$Viscoussensor2) > 0.99?1 : 0 \quad \text{(B.5)}$$

Bibliography

[1] A. Betz. A method for the direct determination of wing-section drag. *Zeitshrift fur Flugtechnik und Motorluftschiffahrt*, 1925.

[2] C. Fournis. Aerodynamic force prediction and breakdown using the lamb vector in steady compressible flows. *Ph.D. thesis, Sorbonne Université*, 2021.

[3] B. Jones. Measurement of profile drag by the pitot-traverse method. *British ARC R&M No. 1688*, 1936.

[4] M. Méheut. Évaluation des composantes phénoménologiques de la traînée d'un avion à partir de résultats expérimentaux. *Ph.D. thesis, Université de Lille*, 2006.

[5] K. Oswatitsch. Gas dynamics. *Academic Press Inc.*, 1956.

[6] L. Paparone and R. Tognaccini. Computational fluid dynamics-based drag prediction and decomposition. *AIAA JOURNAL Vol. 41, No. 9*, 2003.

[7] Siemens. Cfd simulation. `https://www.plm.automation.siemens.com/global/it/our-story/glossary/cfd-simulation/67873`. 2022.

[8] H. Toubin. Prediction and phenomenological breakdown of drag for unsteady flows. *Ph.D. thesis, Pierre et Marie Curie University*, 2015.

[9] H. Toubin and D. Bailly. Development and application of a new unsteady far-field drag decomposition method. *AIAA AVIATION conference, Atlanta*, 2014.

[10] J. Van der Vooren and D. Destarac. Drag/thrust analysis of a jet-propelled transonic transport aircraft: Definition of physical drag components. *Aerospace Science and Technology, vol. 8*, 2004.

[11] J. Van der Vooren and J.W. Slooff. Cfd-based drag prediction: State-of-the-art, theory, prospects. *Lecture Notes of AIAA Professionnal Studies Series, Portland*, 1990.

Personal acknowledgement

I would like to end this work of Thesis by making my personal acknowledgement in Italian.

Ringrazio il Professor Domenic D'Ambrosio che grazie al suo corso di Fluidodinamica Computazionale ha permessso di appassionarmi a questa disciplina e quindi di poter svolgere il lavoro di Tesi Magistrale.

Ringrazio Manuel che durante tutto il lavoro è sempre stato gentile e disponibile per chiarimenti e nell'approfondire tematiche a me inizialmente sconosciute grazie alla sua pazienza e alla sua conoscenza.

Ringrazio il Politecnico di Torino che è stato come la mia seconda casa durante questo percorso e tutti i miei colleghi con cui abbiamo condiviso i momenti più duri, ma anche i momenti più belli, in particolare Alberto e Gabriele.

Ringrazio tutti i miei amici e tutte le persone che sono state presenti in questo viaggio, in particolare Karim e mio cugino Denis.

Ringrazio i miei genitori che con i loro sacrifici mi hanno permesso di seguire questo percorso e di farmi sentire a mio agio anche nei momenti di difficoltà.

Ringrazio infine mio fratello maggiore Simone, Ingegnere Aerospaziale come me, che mi ha sempre guidato a fare la scelta giusta e a non mollare mai di fronte a nessuna sfida.